

## EIC HSR BPM Button Pickup Analysis

M. Wendt

July 2025

Electron-Ion Collider  
**Brookhaven National Laboratory**

**U.S. Department of Energy**  
USDOE Office of Science (SC), Nuclear Physics (NP)

Notice: This technical note has been authored by employees of Brookhaven Science Associates, LLC under Contract No. DE-SC0012704 with the U.S. Department of Energy. The publisher by accepting the technical note for publication acknowledges that the United States Government retains a non-exclusive, paid-up, irrevocable, world-wide license to publish or reproduce the published form of this technical note, or allow others to do so, for United States Government purposes.

## **DISCLAIMER**

This report was prepared as an account of work sponsored by an agency of the United States Government. Neither the United States Government nor any agency thereof, nor any of their employees, nor any of their contractors, subcontractors, or their employees, makes any warranty, express or implied, or assumes any legal liability or responsibility for the accuracy, completeness, or any third party's use or the results of such use of any information, apparatus, product, or process disclosed, or represents that its use would not infringe privately owned rights. Reference herein to any specific commercial product, process, or service by trade name, trademark, manufacturer, or otherwise, does not necessarily constitute or imply its endorsement, recommendation, or favoring by the United States Government or any agency thereof or its contractors or subcontractors. The views and opinions of authors expressed herein do not necessarily state or reflect those of the United States Government or any agency thereof.

# EIC HSR BPM Button Pickup Analysis

D. Gassner, F. Micolon, M. Wendt

*Brookhaven National Laboratory, Upton, NY, USA*

(Dated: July 23, 2025)

## Abstract

The Electron-Ion Collider (EIC) project at the Brookhaven National Laboratory (BNL) will reuse most of the components of one of the hadron storage rings of the Relativistic Heavy Ion Collider (RHIC) for the new EIC Hadron Storage Ring (HSR). To cope with the higher beam intensity in the HSR, a beam screen will be inserted into the superconducting arc sections of RHIC vacuum chamber, which is incompatible with the existing RHIC cold stripline beam position monitors (BPM). Therefore, a new, compact button-style BPM was designed for the HSR, which builds upon the cross-section geometry of the HSR beam screen and tries to meet the requirements of the HSR beam position measurement, while fitting into the space inside the cryostat between superconducting RHIC quadrupole and dipole magnets.

In this document we analyze and compare two different arrangements of the BPM button-style electrodes in the BPM housing wrt. the position sensitivity and non-linearities, the beam-induced RF heating effects, and the expected resolution of the BPM, in particular for the HSR operation with large horizontal beam displacements.

## I. INTRODUCTION

The superconducting (SC) arcs of the EIC Hadron Storage Ring (HSR) will be equipped with 240 new button-style beam position monitor (BPM) pickups, located near the interface between SC quadrupole and dipole magnets. They will be used to replace the to-be-shielded RHIC stripline BPMs and have the same cross-section as the new beam-screen, which will be inserted into the existing RHIC vacuum chambers. These new button BPM pickups are passive cooled in the liquid He cryostat and will have an operational ambient temperature of approximately 10...20 K.

To act as BPM, each pickup is equipped with four symmetrically arranged button-style pickup electrodes, which interact electromagnetically with the beam field and deliver signals that are proportional to the bunched beam intensity and transverse position, circulating in the HSR. Figure 1 shows a highly simplified schematic view of the major hardware components for a specific BPM station:

- A *button BPM* pickup, being part of the accelerator vacuum chamber, located inside the HSR arc cryostat.
- Four *coaxial cables*, i.e. signal transmission-lines, to transfer the four BPM signals to the BPM electronics. In practice each of this cable transmissions is divided in at least three sections, a dedicated 60 inch long, radiation and cryo-temperature compatible SiO<sub>2</sub> coaxial cable inside the cryostat, a up to 240 m long low-loss RF cable and a short coaxial patch cable. The matching of the signal delay, i.e. the cable length, of the four cables may be important.

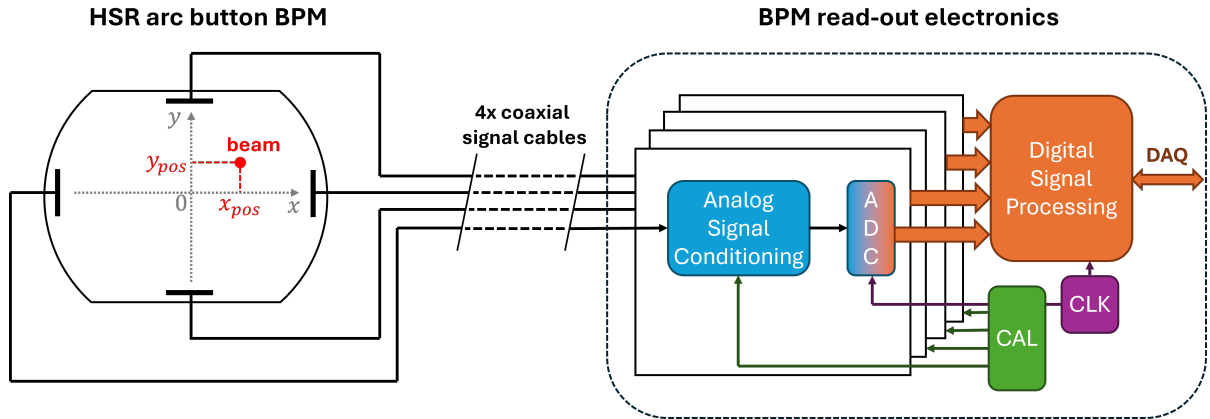


Figure 1. HSR BPM hardware schematics.



- A 4-channel *BPM read-out electronics*, preferable installed outside the accelerator to avoid damage and single event effects (SEE) of the electronics due to the ionizing radiation. This electronics system conditions the button signals, digitizes them, and after further signal processing and decimation of the raw data, provides a beam intensity independent beam position value on a turn-by-turn, bunch-by-bunch, or on a time-averaged (for beam orbit measurement and feedback purposes) basis, calibrated to millimeter.

For the HSR BPMs, as well as for all other BPM pickups in the EIC accelerator complex, we can assume the beams as relativistic,  $\beta \approx 1$ , with the beam field in the vacuum chamber being a purely transverse electromagnetic (TEM). Under this condition the beam induced image charges on each of the four button electrodes produce a signal voltage:

$$\begin{aligned} V_{elec}(x, y, f) &= s(x, y) Z_{elec}(f) I_{beam}(f) \\ \Rightarrow v_{elec}(x, y, t) &= s(x, y) \int_{-\infty}^{+\infty} Z_{elec}(f) I_{beam}(f) e^{i2\pi ft} df \end{aligned} \quad (1)$$

with  $I_{beam}(f)$  being the *Fourier* transform of the bunched beam current  $i_{beam}(t)$  and  $Z_{elec}(f) = Z_{button}(f)$  the *transfer impedance* of the button electrode, which can be estimated from the mechanical dimensions:

$$Z_{button}(\omega) = \phi R_{load} \frac{\omega_1}{\omega_2} \frac{i\omega/\omega_1}{1 + i\omega/\omega_2} \quad (2)$$

with:

$$\begin{aligned} \omega_1 &= \frac{1}{R_{load} C_{button}} \propto 1/\text{time constant} \\ \omega_2 &= \frac{c}{2r} \propto 1/\text{transit time} \end{aligned}$$

for the angular frequency  $\omega = 2\pi f$  and a button diameter  $2r$ . For the HSR BPM buttons, as well as for almost any button BPM pickup, the resistive *load impedance* is equal to the characteristic impedance of the coaxial signal cable,  $R_{load} = Z_0 = 50 \Omega$ . The *button capacitance*  $C_{button}$  depends for the size and geometric details of the button electrode, and its surroundings, and was determined by a numerical analysis for a generalized HSR BPM button geometry.  $\phi$  in Eq. (2) relates to a *coverage factor*, defined by the portion of the image charges induced on the BPM button wrt. the total image charges in that area of the beam pipe, assuming the beam being in the center of the beam pickup ( $x = y = 0$ )! For simple cross-section geometries like a circular vacuum chamber,  $\phi$  can be approximated

by the geometric coverage area of the button, for the HSR BPM chamber with its more complicated cross-section geometry a numerical analysis was performed.



Please note, Eq. (1) is nothing else than *Ohm's* law. However, there exist different definitions for the term *transfer impedance* in connection with beam pickups!

The beam current in Eq. (1) could be defined as:

$$i_{beam}(t) = \langle I_{DC} \rangle + 2\langle I_{DC} \rangle \sum_m^{\infty} A_m \cos(m\omega t)$$

with  $\langle I_{DC} \rangle = en/T$  ( $en = q_{beam}$  and  $T = 2\pi/\omega = k/f_{RF}$  relating to the bunch spacing or revolution period  $T$ ) and  $A_m$  being a harmonic amplitude factor (assuming bunches of same intensity and equally spaced!), e.g.  $A_m = \exp[(m\omega\sigma)^2/2]$  for a *Gaussian* bunched beam. However, in practice the definition of the bunch current  $i_{bunch}(t)$  as stimulus signal is more convenient, as the beam pickup electrode is a LTI system (linear and time-invariant), and the superposition principles can always be applied. For the HSR we can assume *Gaussian* bunches in collision operation:

$$i_{Gauss}(s) = \frac{en}{\sigma_s \sqrt{2\pi}} e^{-\frac{1}{2}(\frac{s}{\sigma_s})^2} \quad \equiv \quad i_{Gauss}(t) = \frac{en}{\sigma_t \sqrt{2\pi}} e^{-\frac{1}{2}(\frac{t}{\sigma_t})^2} \quad (3)$$

with a RMS bunch length of  $\sigma_s \approx 60 \text{ mm} \equiv \sigma_t \approx 200 \text{ ps}$  and a bunch charge of  $q_{bunch} = en$ . In the frequency domain Eq. (3) results in:

$$I_{Gauss}(f) = ene^{-2(\pi f \sigma_t)^2} \quad (4)$$



Please note, for beams in the HSR at injection energy, during cooling and RF reformatting, the bunches in the HSR are **not *Gaussian***!

Finally in Eq. (1),  $s(x, y)$  refers to a *sensitivity function* that depends on the transverse distance between beam and electrode, preferable given in  $(x, y)$  *Cartesian* coordinates wrt. center of the BPM pickup, see also Fig. 1. The sensitivity function varies  $0 \leq s(x, y) \leq 1$ , and for a centered beam  $x = y = 0$  is equivalent to the coverage factor,  $s(0, 0) = \phi$ .



While the BPM button indeed is a LTI system, i.e. the button output voltage is always proportional to the beam or bunch current,  $v_{button} \propto i_{beam}$ , the position sensitivity  $s(x, y)$  is a **non-linear** function of the  $(x, y)$  transverse beam position!

A beam intensity independent position measurement is performed by *normalization*, using all signals of four symmetrically arranged BPM button electrodes. Different types of normalization exist, with the signal levels measured and digitized separately (see Fig. 1), the popular *difference-over-sum* (DOS or  $\Delta/\Sigma$ ) method will be applied for the HSR BPMs:

$$pos. = f \left( \frac{v_A - v_B}{v_A + v_B} \right) \quad (5)$$

with  $pos.$  being the horizontal or vertical beam position and  $v_A, v_B$  the output voltage signals of a pair of BPM buttons symmetrically arranged in the horizontal or vertical plane.

In theory we could now analyze the non-linear position characteristics of the button BPM pickup by assigning  $v_{A,B} \equiv v_{elec}$ , i.e. Eq. (1) into Eq. (5), and scanning the transverse  $(x, y)$  space. Even making use of some symmetry conditions, this would be a very time consuming numerical calculation for the BPM pickup! Fortunately Eq. (1) separates the frequency dependent, but not position dependent transfer characteristic  $Z_{elec}(f)$  from the frequency independent, position characteristic  $s(x, y)$  of the button electrode, allowing not only to separate the analysis of the BPM button output signal waveform from its position behavior, but by applying the *reciprocal theorem* is also an efficient way to compute the position characteristic of the entire BPM pickup.



Again, this is only true for broadband BPM pickups, such as button, stripline or split-plane BPMs without any resonances (eigen-modes) within the bunched-beam spectrum measured by the BPM read-out electronics, and only for those BPM operating with relativistic beams! For, e.g. cavity BPMs, or for broadband BPMs operating with non-relativistic beams ( $\beta \ll 1$ ) Eq. (1) does not apply!

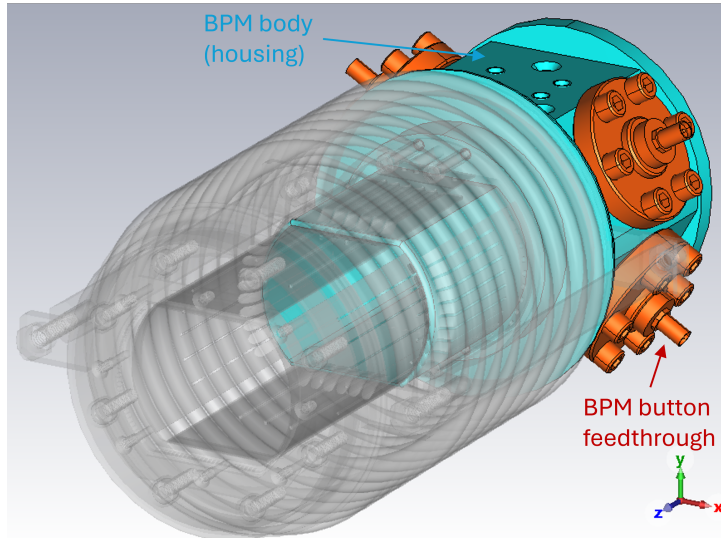


Figure 2. STEP file model of the HSR corner BPM.

## II. THE HSR BUTTON BPM FOR THE CRYOGENIC ARC SECTIONS

The analysis of the HSR BPM is based on numerical methods which require a model of the physical geometry, for some calculations also the electrical properties of the materials are used. Figure 2 shows the HSR button BPM for the SC arc sections as visualization of the mechanical design STEP file, transparently shown are the bellows, beam-screen and other non-relevant parts.

The numerical analysis of the HSR BPM is divided in two steps:

1. As electromagnetic analysis, i.e. the interaction between the EM-field of a beam bunch of given parameters (bunch charge, bunch length and shape, and bunch velocity) and the HSR BPM pickup structure using the *CST Studio* wakefield solver, for a beam traveling in the center of the beam pipe / pickup, or with at a given transverse  $(x, y)$  offset. This analysis delivers the output signal response at one or several BPM button electrodes into a perfect  $50\ \Omega$  termination (load impedance).
2. As electrical circuit analysis of the BPM signal transmission and conditioning, starting from the BPM button through the coaxial cables up to the front-end part of the read-out electronics (analog signal conditioning and ADC) using the *Keysight Pathwave ADS* transient solver. This analysis utilizes the BPM button output signal given by the CST wakefield simulation, as well as other BPM pickup characteristics provided by *CST Studio* simulations, e.g. the button capacitance  $C_{button}$ , to model

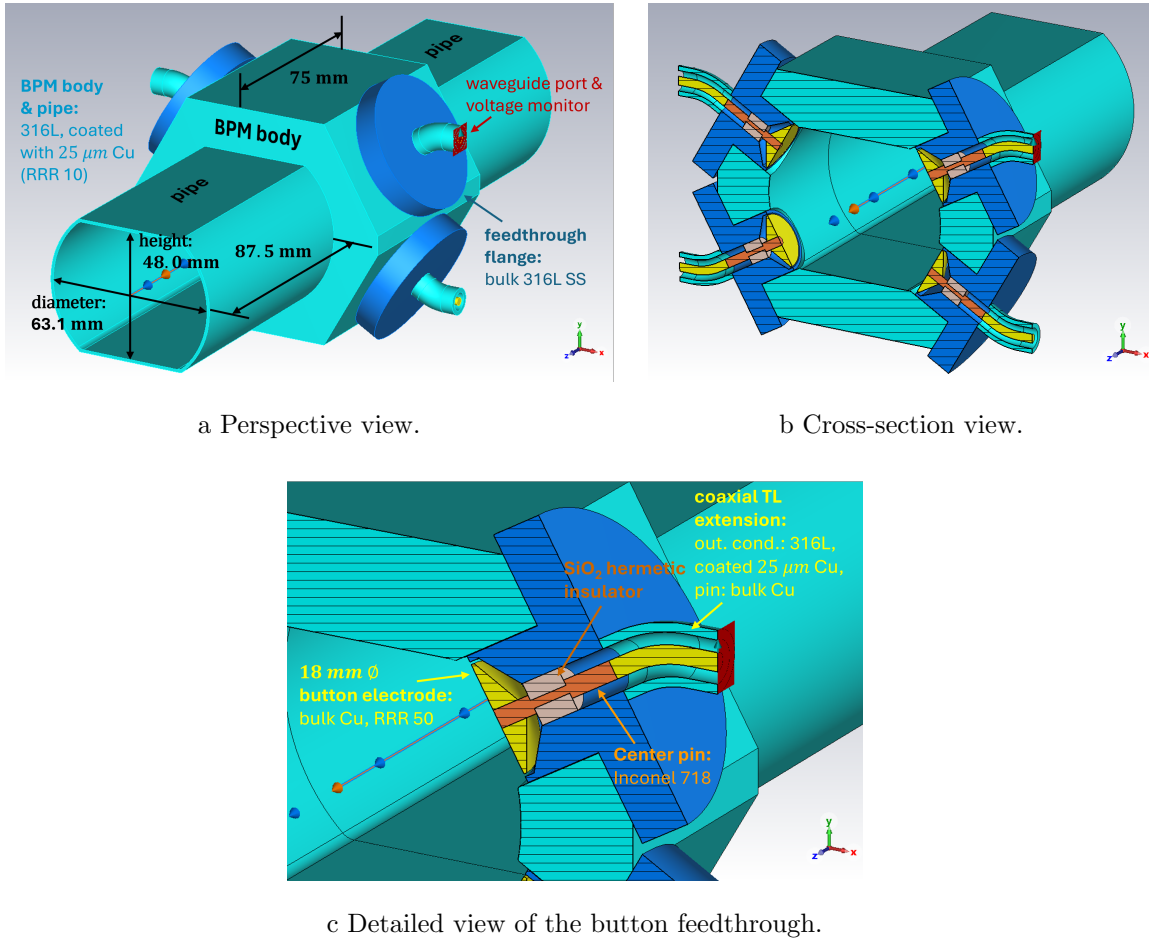


Figure 3. CST Studio 3D parametric model of the HSR corner BPM.

the button electrode as equivalent circuit.

For the electromagnetic analysis the 3D geometry given as mechanical model STEP file (Fig. 2) was reproduced as parametric 3D geometry, including the material properties in *CST Studio*. This “CST model geometry”, see Fig. 3, uses the same dimensions as the STEP file geometry, e.g. the mixed circular/rectangular shape of beam pipe (inner diameter 63.1 mm, inner height 48.0 mm), etc., but with some simplifications and removing non-relevant details like mounting screws, etc. This CST geometry served for both, the BPM button signal analysis (CST wakefield solver), i.e. the button electrode output signal  $v_{elec}$  for a given bunch signal  $i_{bunch}$ , for the wakefield analysis (CST wakefield solver, i.e. the beam induced power losses, and for the S-parameter analysis (CST transient solver), i.e. a time-domain reflectometry (TDR) of S11, e.g. to evaluate the button capacitance  $C_{button}$ .

The position characteristic of the broadband HSR button BPM pickup is independent

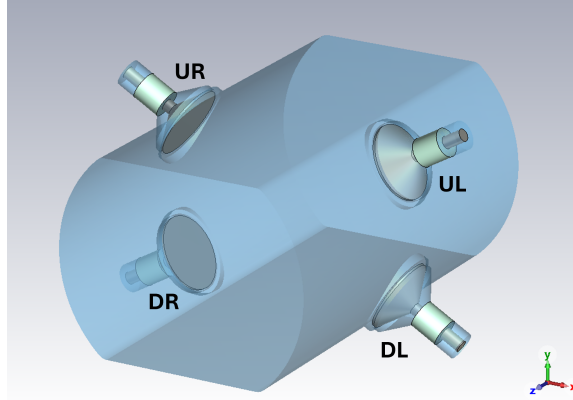


Figure 4. Simplified 3D geometry of the HSR corner BPM for the electrostatic analysis.

from the bunch signal shape, respectively the frequency content, see also Eqs. (2) and (5). Therefore, the position characteristic was analyzed as electrostatic problem by numerically solving the *Laplace* equation using a simplified, loss-free parametric 3D model geometry, again implemented in CST, see Fig. 4.

Notably, the four BPM buttons are symmetrically arranged in HSR circular/rectangular beam-screen aperture under an angle of  $30^\circ$ , which we call the *HSR corner BPM* as the BPM buttons are located in the corners of the circular/rectangular shape, see Figs. 2 to 4. The following numerical analysis shows, beside some advantages, also some shortcomings for this type of BPM button arrangement, therefore, the more popular electrode arrangement for hadron BPMs along the horizontal and vertical axis was studied as well, which we call the *HSR orthogonal BPM*, see Fig. 5.

### III. POSITION CHARACTERISTIC OF THE HSR BPM PICKUP

#### A. Theoretical background

Without proof, the electromagnetic (EM) field of a charged particle (point charge) traveling at relativistic velocity,  $\beta = v/c \approx 1$ , inside the metallic (conductive) beam pipe has only transverse components (TEM field), and the coupling between the charged particle  $\rho = q \delta(\mathbf{r} - \mathbf{r}_0)$  and a BPM electrode can be simplified to an electrostatic problem, by solving the *Poisson* equation in the reference frame of the particle:

$$\nabla^2 \Phi(\mathbf{r}) = -\rho/\varepsilon_0 \quad (6)$$

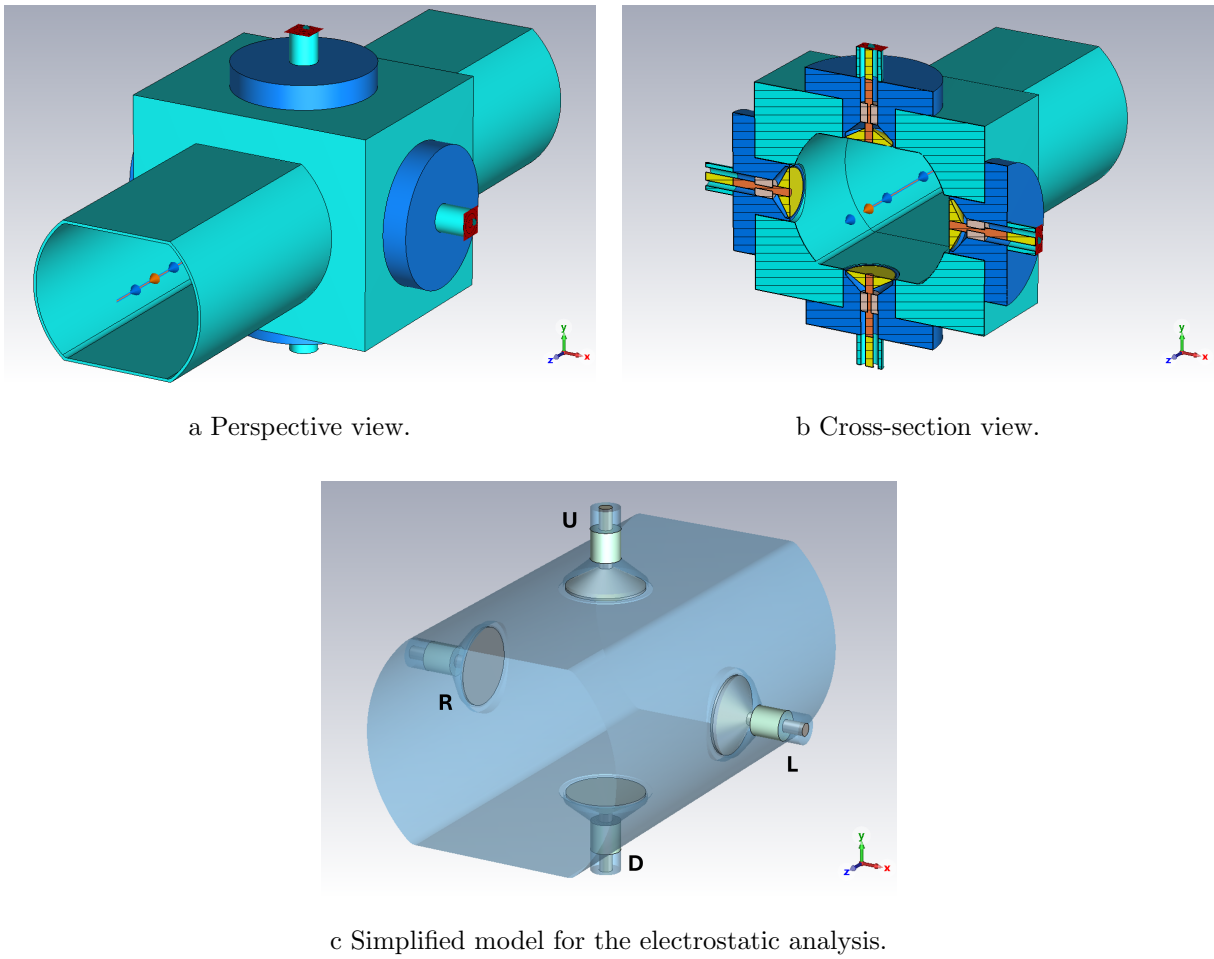


Figure 5. CST Studio 3D parametric model of the HSR orthogonal BPM.

In the following we neglect the the transverse size of the bunched beam, assuming  $\sigma_{x,y} \ll a$ , taking the beam as line charge density distribution  $\lambda(z - ct) = i_{beam}(t)$  with effectively  $\sigma_{x,y} = 0$  and with  $a$  being the transverse beam pipe aperture, e.g. this would be the diameter for a beam pipe with circular cross-section<sup>1</sup>.

Figure 6 illustrates a possible solution of electrostatic field problem for the HSR corner BPM with a beam, indicated as line charge with a transverse beam position  $x_{beam} = 15$  mm,  $y_{beam} = 5$  mm (see Fig. 6a), with Fig. 6b showing the electric field distribution of the beam line charge in the  $z = 0$   $xy$ -plane as numerical solution of Eq. (6) using the electrostatic solver of the *CST Studio* software.

To analyze the normalized horizontal and vertical position characteristic following Eq. (5), we would have to monitor the image charges on each of the four BPM electrodes, equivalent to  $s(x, y)$  in Eq. (1), and scan the transverse beam line charge position in the

<sup>1</sup> Please note, the HSR beam pipe does not have a circular cross-section.

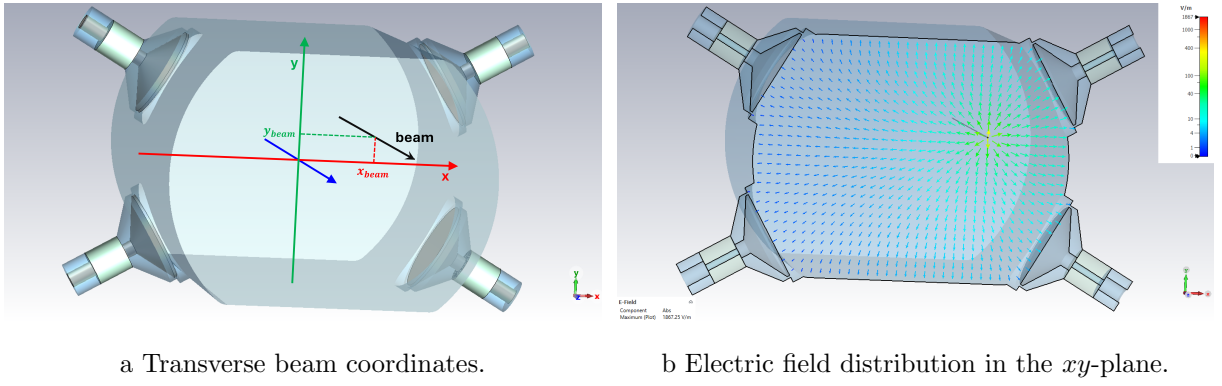


Figure 6. Solution of the electrostatic beam field problem for the HSR corner BPM.

$xy$ -plane  $x_{min} < x_{beam} < x_{max}$ ,  $y_{min} < y_{beam} < y_{max}$ . This time-consuming procedure can be simplified by applying *Green's* reciprocity theorem

$$\int_V \phi_1 \rho_2 dV + \int_S \phi_1 \sigma_2 da = \int_V \phi_2 \rho_1 dV + \int_S \phi_2 \sigma_1 da \quad (7)$$

with  $\phi_i$  being the potentials, and  $\rho_i$  and  $\sigma_i$  the volume and surface charge densities, respectively. Applied to the BPM case we use  $\phi_1 = \phi_{elec}(\mathbf{r})$  as scalar potential for the electrode set to a fixed voltage potential, e.g.  $\mathcal{V} = 1$  V, while putting all other surfaces to ground potential. For this case Eq. (7) simplifies to

$$\int_V \phi_{elec}(\mathbf{r}) \rho_2(\mathbf{r}) dV = -\mathcal{V} q_{elec} \quad (8)$$

with  $q_{elec}$  being the total charge on the button electrode. Assuming  $\rho_2$  is a point charge  $q$  at  $(\mathbf{r}_0)$ , Eq. (8) retrieves the value of the scale potential  $\phi_{elec}(\mathbf{r}_0)$  at that location

$$q_{elec} = -\frac{q \phi_{elec}(\mathbf{r}_0)}{\mathcal{V}} \quad (9)$$

demonstrating that  $\phi_{elec}(\mathbf{r}_0)$  indeed is equivalent to  $s(x, y)$  in Eq. (2), and is proportional to the induced surface charge on the button electrode  $q_{elec}$ . This leads to a solution of the *Laplace* equation

$$\nabla^2 \Phi_{elec}(\mathbf{r}) = 0 \quad (10)$$

by putting the electrode to a fixed voltage potential  $\mathcal{V}$  and all other surfaces being grounded (see Fig. 7), but with the caveat that the beam line charge and vacuum chamber are 2D objects in the  $xy$ -plane, while the button electrode is a 3D object.

Figure 8 illustrates the result of Eq. (10) for the HSR corner BPM with the upper left (UL) button electrode set to a fixed potential  $\mathcal{V} = 1$  V as shown in Fig. 7. Figure 8a



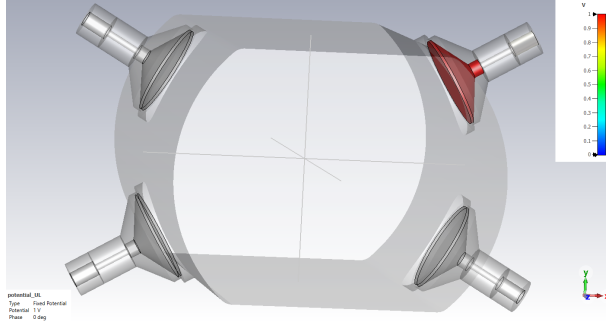


Figure 7. HSR corner BPM with the upper left (UL) button set to  $\mathcal{V} = 1$  V.

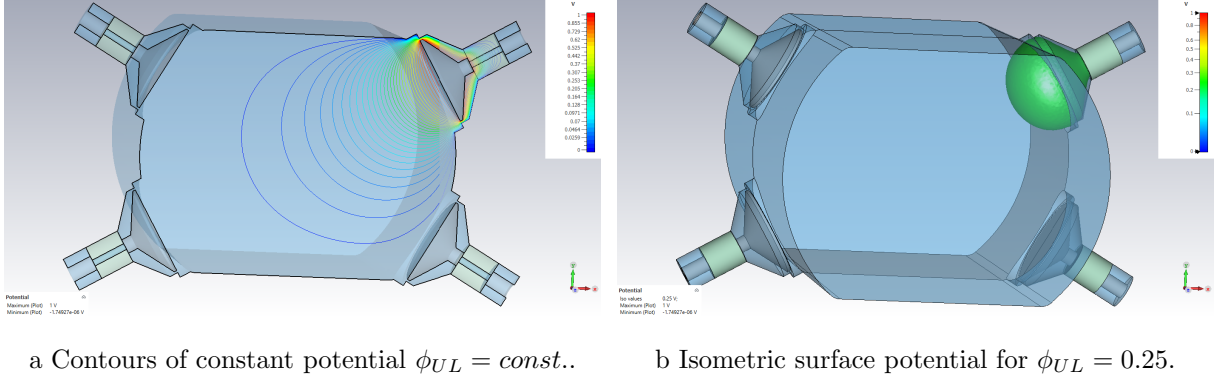


Figure 8. Scalar potential  $\phi_{UL}(\mathbf{r})$  for the UL electrode of the HSR corner BPM.

shows  $\phi_{UL}(x, y) = const.$  in the  $x, y$ -plane ( $z = 0$  cross-section) and Fig. 8b shows the result for  $\phi_{UL}(x, y, z) = 0.25$  as isometric surface.

In most cases the position characteristic of broadband button-style BPMs have been analyzed as purely 2D electrostatic problem, i.e. in the  $xy$  symmetry plane. Unfortunately, a detailed study demonstrates that this is an oversimplification of the 3D nature of the button electrodes and their coupling to the beam, and leads to systematic errors evaluating the position characteristic. Comparing 2D and 3D electrostatic analysis' of circular button electrodes and long stripline electrodes of the same  $xy$  cross section shape shows that we need to use the 3D equipotential result of Eq. (10) as basis for a correct result. The induced image charge on the button electrode is then calculated from the 3D scalar potential  $\phi_{elec}(x, y, z)$  as

$$q_{elec} \propto \phi_{elec}(x, y) = \frac{\int_{z=z_{min}}^{z_{max}} \phi_{elec}(x, y, z) dz}{d_{eff}} \quad (11)$$

except for the constant factor  $-q/\mathcal{V}$ , with  $d_{eff} = d_{button} + g$  being the “effective” button diameter which includes the half gap width  $g$ . Using Eq. (11) and and setting  $\mathcal{V} = 1$  V

also results in the correct value for the coupling sensitivity  $s(x, y)$  between beam and button electrode in Eq. (2).

## B. Numerical calculation procedures

The normalized, i.e. beam intensity independent position characteristic is now calculated numerically for the two HSR BPM button electrode configurations, following Eq. (5) and the procedure described in the previous section:

$$\begin{aligned} \phi_h &= \frac{(\phi_{UR} + \phi_{DR}) - (\phi_{UL} + \phi_{DL})}{\Sigma\phi} & \phi_v &= \frac{(\phi_{UR} + \phi_{UL}) - (\phi_{DR} + \phi_{DL})}{\Sigma\phi} & \text{corner BPM} \\ \phi_h &= \frac{\phi_R - \phi_L}{\phi_R + \phi_L} & \phi_v &= \frac{\phi_U - \phi_D}{\phi_U + \phi_D} & \text{orthog. BPM} \end{aligned} \quad (12)$$

with  $\Sigma\phi = \phi_{UR} + \phi_{DR} + \phi_{UL} + \phi_{DL}$  and the indices UR, UL, DR and DL indicating the up-right, up-left, down-right and down-left button electrodes for the HSR corner BPM (see also Fig. 4) and R, L, U, and D the up, down, right and left button electrode for the HSR orthogonal BPM (see also Fig. 3c).



Please note, the right/left labels are defined in beam (+z) direction.

Due to the 2-fold symmetry of the HSR corner BPM, it is sufficient to solve Eq. (10) for only one button electrode, here for the UL electrode with the potential set to  $\mathcal{V} = 1$  V as shown in Fig. 7. The computation was performed using the electrostatic solver (ES) of the *CST Studio* software with a high number of tetrahedral mesh cells ( $\sim 5 \times 10^5$ ), and making use of the symmetries, i.e. calculating 1/8 of the structure by applying magnetic symmetry boundaries. For the HSR orthogonal BPM the 1-fold symmetry requires separate computations for the R and for the U button electrodes.

The 3D scalar potential result of *CST* ES (Potential [Es]),  $\phi_{elec}(x, y, z)$ , is then sampled in steps of  $\Delta x = \Delta y = \Delta z = 0.5$  mm and stored as ASCII text file, so we have  $\phi_{UL}(x, y, z)$  for the HSR corner BPM and  $\phi_R(x, y, z)$  and  $\phi_U(x, y, z)$  for the HSR orthogonal BPM.

These files are now post-processed using the *Mathematica* software, and as an initial step we compute the 2D scalar potential by numerical integration along the  $z$ -axis and normalization with  $d_{eff} = 18.4658$  mm following Eq. (11) to get  $\phi_{UL}(x, y)$  for the corner

BPM, and  $\phi_R(x, y)$  and  $\phi_U(x, y)$  for the orthogonal BPM. The missing scalar potentials for the other electrodes are simply generated by rearranging the discrete matrix elements of those scalar potentials accordingly to the symmetry conditions, e.g. inverting the  $x$ -vector to get  $\phi_L(x, y) = \phi_R(-x, y)$ .

Having now the scalar potentials of all electrodes as vector matrix at hand, step size 0.5 mm, we simply compute the normalized horizontal and vertical position characteristic,  $\phi_h$  and  $\phi_v$ , for the corner and orthogonal BPM following Eq. (12). For a better follow up analysis, the results are then approximated by an *interpolating function* in *Mathematica*.

### C. Results

The beam-to-electrode coupling sensitivities for a centered beam ( $x = y = 0$  mm) are found as

$$\begin{aligned} \text{corner BPM: } & \phi_{UR}(0, 0) = \phi_{UL}(0, 0) = \phi_{DR}(0, 0) = \phi_{DL}(0, 0) = 0.048697 \\ \text{orthogonal BPM: } & \begin{cases} \phi_R(0, 0) = \phi_L(0, 0) = 0.0532306 \\ \phi_U(0, 0) = \phi_D(0, 0) = 0.11976 \end{cases} \end{aligned}$$

which are equivalent to the sensitivity factor  $s$  in Eq. (2) and are important to calculate the output voltage signal of the button electrodes. In simple words, the corner BPM electrodes couple out  $\sim 5\%$  of the image charges for a centered beam, approximately the same is true for the horizontal electrodes of the orthogonal BPM. The vertical button of the orthogonal BPM are much closer to the beam, therefore the coupling is  $\sim 10\%$  if the beam is in the center.

Figures 9 and 10 summarize the results of the normalized  $\Delta/\Sigma$  horizontal and vertical position characteristic for both BPM button electrode configurations, the corner and the orthogonal BPM. The parametric plots, Figs. 9a, 9d, 10a and 10d, show lines of  $\Delta/\Sigma = \text{const.}$ , visualizing the non-linear behavior wrt. the beam position. In other words, if the beam position would move on one of these lines, without further correction the BPM would report the always same horizontal or vertical beam position. Evidently, the nonlinearities are more pronounced for the corner BPM configuration, in particular for the vertical position measurement. Also indicated (dashed rectangle) is the maximum anticipated operational range of the BPM, horizontal  $\pm 23$  mm and vertical  $\pm 2$  mm. The  $\Delta/\Sigma$  plots, Figs. 9b, 9e, 10b and 10e, illustrate the position behavior along the axis of

interest, for beam offset of 0, 5 and 10 mm in the other axis. Figures 9c, 9f, 10c and 10f show the gradient of those  $\Delta/\Sigma$  plots, which indicates the position sensitivity of the BPM button configuration. For beams near the center the sensitivity in the horizontal plane is similar for both button configurations, in the vertical plane evidently the orthogonal button arrangement is preferable.

For large horizontal beam displacements,  $x \approx \pm 20$  mm, as expected for proton beams in the HSR operating at a beam energy of 275 GeV or 100 GeV, the horizontal position sensitivity is substantially reduced,  $\sim 5\times$ , regardless of the type of the button configuration, see Figs. 9c and 10c. This also means the precision (resolution) of the measurement will be reduced by approximately the same factor. However, the orthogonal BPM button configuration allows a “trick”, using the two vertical electrodes U and D as a *virtual* horizontal electrode. E.g. for large positive horizontal beam trajectories,  $E_p \approx 275$  GeV, we would use the U and D, and the R button electrodes for the horizontal beam position measurement, which is simply possible as the BPM read-out electronics continuously acquires and analyses all four individual BPM button signals simultaneously, see Fig. 1. For this “trick”, the position characteristic is calculated as

$$\phi_{h,trick} = \frac{(\phi_U + \phi_D)/2 - \phi_L}{(\phi_U + \phi_D)/2 + \phi_L} \quad (13)$$

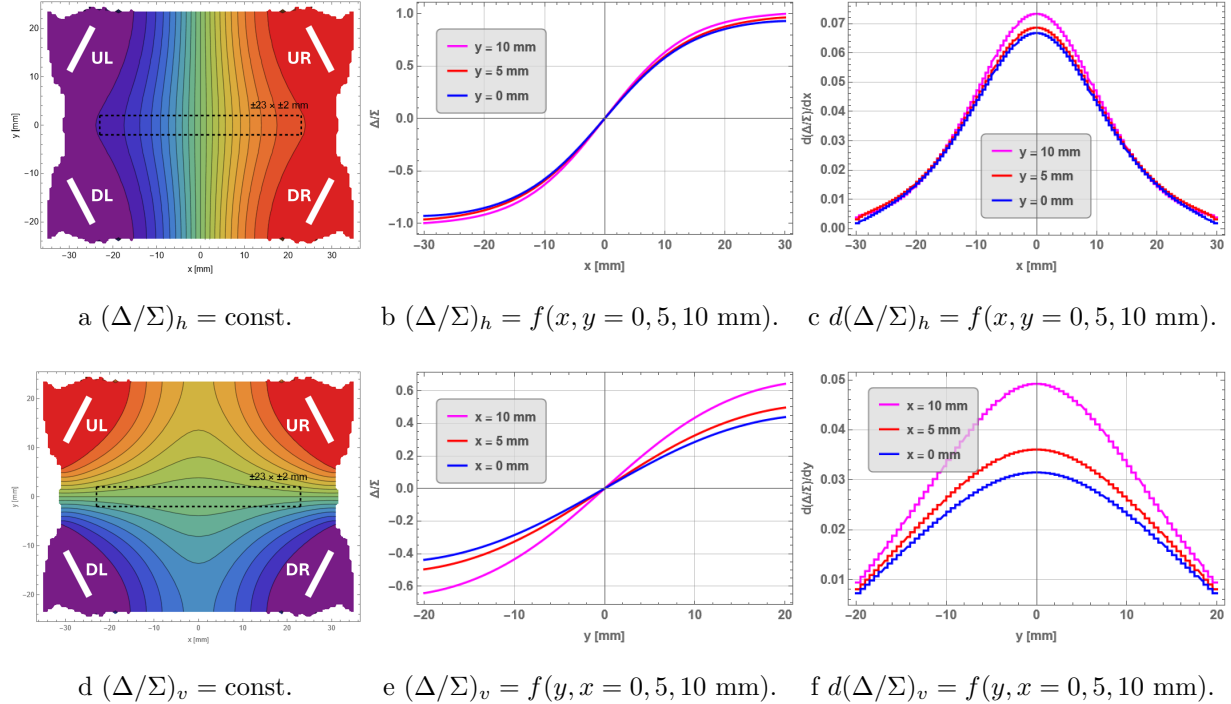


Figure 9. Normalized position characteristics of the HSR corner BPM.

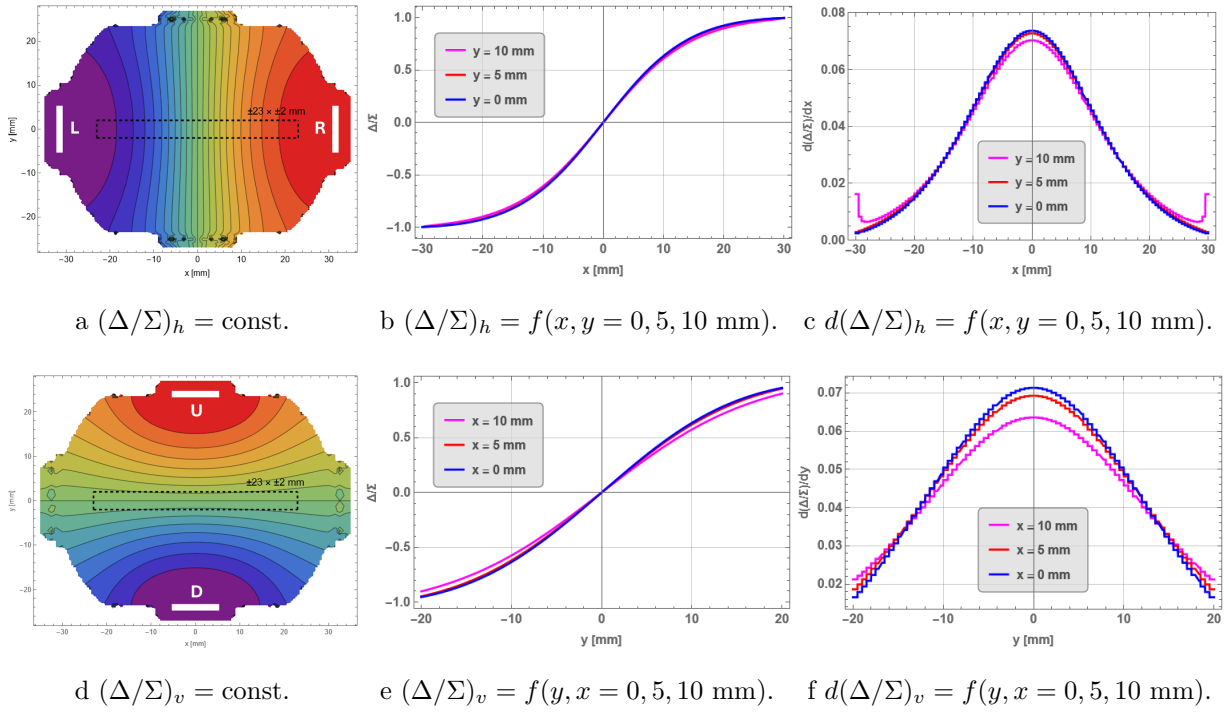


Figure 10. Normalized position characteristics of the HSR orthogonal BPM.

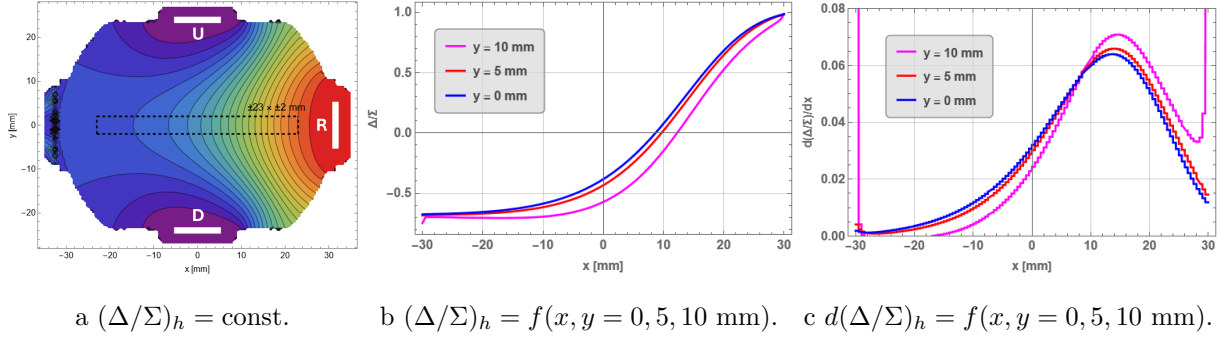
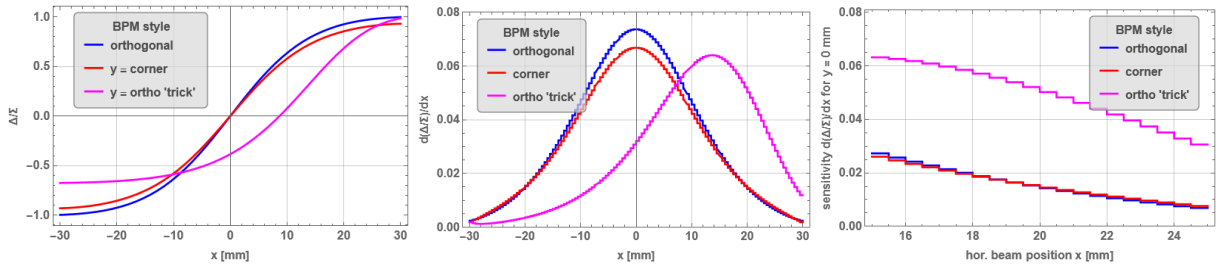


Figure 11. Normalized hor. position characteristics of the orthogonal BPM “trick” configuration.

and Fig. 11 illustrates the result. At a horizontal beam offset of +20 mm the loss of sensitivity is less severe,  $\sim 1.5\times$ , however, the nonlinearities are still substantial.

Figure 12 illustrates the advantage of the “trick” configuration for large horizontal offsets comparing the normalized  $\Delta/\Sigma$  horizontal position characteristic for all three measurement options, Fig. 12c zoomed into the range of interest for the gradient  $d(\Delta/\Sigma)_h/dx$  around +20 mm.



a  $(\Delta/\Sigma)_h = f(x, y = 0 \text{ mm})$ .      b  $d(\Delta/\Sigma)_h = f(x, y = 0 \text{ mm})$ .      c  $d(\Delta/\Sigma)_h = f(x, y = 0 \text{ mm})$ ,  
zoomed.

Figure 12. Comparison of the normalized horizontal position characteristic for the different HSR BPM button configurations.

#### IV. CORRECTION OF THE NON-LINEAR POSITION CHARACTERISTIC

The HSR BPM system, as well as all other BPM systems of the EIC complex, will acquire and digitize the signals of each of the four BPM button electrodes separately, as illustrated in Fig. 1. This allows the correction of the non-linear behavior of the BPM pickup position characteristic and the scaling, usually to *millimeters* (mm) within the digital signal processing section of the read-out electronics.

##### A. Theoretical background

###### 1. Linear scaling

The simplest and straightforward method to scale the measured signals from the button electrodes is to apply a linear scaling factor:

$$pos. \approx \frac{1}{k} \frac{A - B}{A + B} \quad (14)$$

with  $A$  and  $B$  being the *count* values of the ADC's proportional to  $v_A$  and  $v_B$  to the signal levels of the horizontal or vertical pair of BPM electrodes.  $k$  is the gradient of  $\Delta/\Sigma = f(x, y)$ , given in  $\text{mm}^{-1}$ , at the center of the beam pipe,  $x = y = 0$  for the axis of interest. For a BPM with circular-cross section of radius  $R_{pipe}$  the gradients for the horizontal and vertical plane are identical, and can be approximated as  $k_x = k_y = k \approx 2/R_{pipe}$ . For the HSR button BPM, e.g. with the orthogonal BPM electrode arrangement, horizontal and vertical gradients are different, however, not as much as the cross-section geometry suggest,  $k_x \approx 0.0736 \text{ mm}^{-1}$  and  $k_y \approx 0.0713 \text{ mm}^{-1}$ , see also Fig. 10.

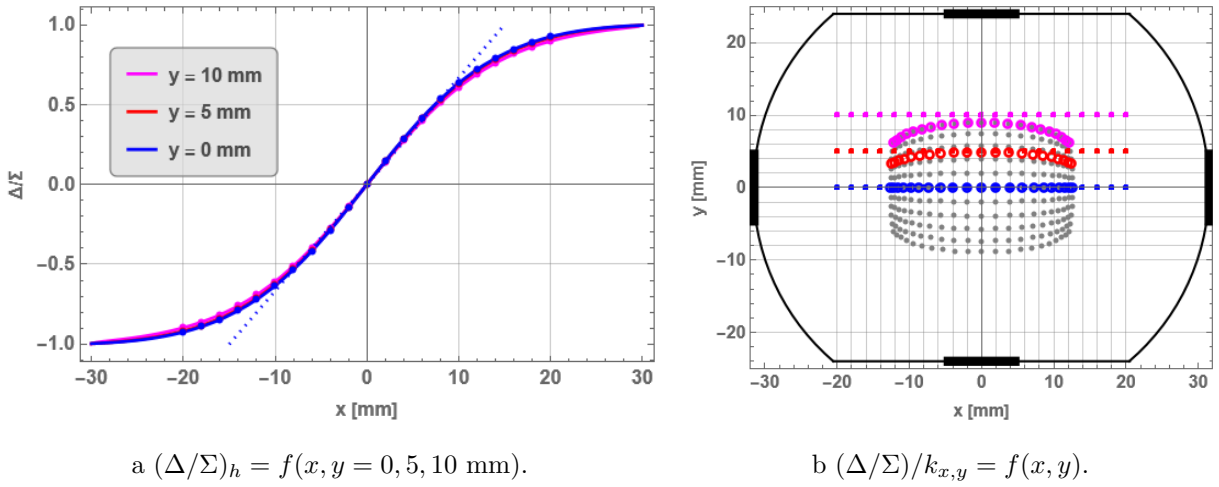


Figure 13. Linear scaling of the HSR orthogonal BPM position characteristic.

Figure 13 illustrates the shortcomings on the linear scaling on the example of the HSR orthogonal BPM. The left-hand side, Fig. 13a, shows  $(\Delta/\Sigma)_h$  for the horizontal plane in the range  $-30 \text{ mm} < x < 30 \text{ mm}$  for vertical beam displacements at  $y = 0, 5, 10 \text{ mm}$ , similar to Fig. 10b, but also indicating  $k_x$  (dotted line) and *points* spaced by  $\delta x = 2 \text{ mm}$  in the range  $-20 \text{ mm} < x < 20 \text{ mm}$  on the traces. The right-hand side, Fig. 13b, shows the result as of the linear scaling with  $k_x$  and  $k_y$  as given above as grid of *points* and *circles* in the  $xy$ -plane, in a range  $-20 \text{ mm} < x < 20 \text{ mm}$ ,  $-10 \text{ mm} < y < 10 \text{ mm}$ . The blue points in Fig. 13a, sampling  $(\Delta/\Sigma)_h = f(x, y = 0)$  at the *true* beam position in steps of  $\delta x = 2 \text{ mm}$ , appear as blue circled measured position values  $(x_{bpm}^{lin}, y_{bpm}^{lin})$  in Fig. 13b. Hardly to distinguish in Fig. 13a, the red and magenta points appear as same colored circled measured position values, now with some vertical offset in Fig. 13b. For reference, the true beam position value  $(x, y)$  for each colored circle value is also indicated in Fig. 13b as colored dot.

To complete the picture, gray points in Fig. 13b map the nominal position values on a 2 mm grid in a  $\pm 20 \times \pm 10 \text{ mm}$  area after applying the linear scaling. Beside a rather small area near the center, the difference, i.e. the *error*, between the true position value  $(x, y)$  and the measured position value based on linear scaling  $(x_{bpm}^{lin}, y_{bpm}^{lin})$  becomes larger with increasing distance to the center. The “shrinking” measurement effect is called *pin-cushion effect*, Fig. 14 shows the absolute error in mm.

## 2. 1D polynomial error correction

A correction of the non-linearities of the BPM position characteristic, which also takes care of the scaling, can be implemented in two ways, by a *look-up table* or by a *polynomial* correction. For the EIC BPMs, including those in the HSR, we consider the polynomial correction, which requires less “house-keeping” and only a small set of correction data, simple in the post-processing.

E.g. for the horizontal axis, let's define the *raw* position data as

$$x_{raw} = f(x) = \left( \frac{\Delta}{\Sigma} \right)_h = \frac{R - L}{R + L} \quad (15)$$

with  $R$  and  $L$  being the count values of the ADC's proportional to  $v_R$  and  $v_L$  to the signal levels of the horizontal pair of BPM electrodes. We can assume Eq. (15) to be a *smooth* function of the true beam position  $x$ , which can be simply inverted:

$$x = f^{-1}(x_{raw}) \quad (16)$$

A *polynomial* of power  $p$  can now be calculated that approximates Eq. (16)

$$x_{bpm}^{1D} = \sum_{i=0}^p (c_i x_{raw}^i) = U_p(x_{raw}) \approx x \quad (17)$$

The polynomial fit approximation is based on a *regression model*, e.g. *least-squares*. Due to the symmetry of the BPM pickup, the even polynomial coefficients in Eq. (17) vanish,  $c_i = 0, \forall i \in 2\mathbb{Z}$ , however, this is not the case for asymmetric situations, like the “trick” BPM. For the vertical axis,  $y_{bpm}^{1D} = U_p(y_{raw})$  in general is a different function, like here

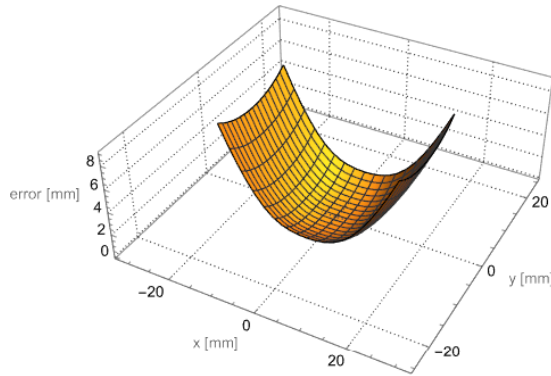


Figure 14. Absolute position error  $|(x_{bpm}^{lin}, y_{bpm}^{lin}) - (x, y)|$  in mm for the corner BPM, following the measurement based on linear scaling.



for the HSR BPM, except for BPM pickups with two-fold symmetry, e.g. with circular cross-section.



An even-order coefficient  $c_0 \neq 0$  corresponds to an BPM offset.

The polynomial converts the raw horizontal (or vertical)  $\Delta/\Sigma$  data directly into a scaled position value in mm. The accuracy of the linearization depends on the power  $p$  of the polynomial, but also on the range of  $f^{-1}(x_{raw})$  to be fitted, as well as on accuracy and data points of the source function  $f(x)$ .

### 3. 2D polynomial error correction

As seen in the next paragraph from the results, the 1D polynomial correction works well along the horizontal or vertical axis, but not so good for the entire  $xy$ -plane. The 2D polynomial correction makes use of the signals of other pair of BPM electrodes, taking the both  $\Delta/\Sigma$  raw data into account for a correction of the position nonlinearities in the entire  $xy$ -plane.

For an arbitrary beam offset  $x, y \neq 0$  within the BPM aperture, the coupling between the raw position acquired by the ADCs as uncorrected  $\Delta/\Sigma$  information and the true  $(x, y)$  beam position can be linked to two functions:

$$\begin{cases} x_{raw} = f(x, y) \\ y_{raw} = g(y, x) \end{cases} \quad (18)$$

which again can be assumed to be smooth and therefore invertible (please note the swap of the variables for  $g$ ):

$$\begin{cases} x = f^{-1}(x_{raw}, y_{raw}) \\ y = g^{-1}(y_{raw}, x_{raw}) \end{cases} \quad (19)$$

We now fit the inverse raw  $\Delta/\Sigma$  position data, Eq. (19) with a 2D *surface* polynomial  $Q_{pq}$  of power  $p$  and  $q$  for both variables, which allows to correct the entangled, non-linear relationship between them and returns an approximation of the true, orthogonal horizontal and vertical beam position:

$$\begin{cases} x_{bpm}^{2D} = \sum_{i,j=0}^{p,q} (c_{ij} x_{raw}^i y_{raw}^j) = Q_{pq}(x_{raw}, y_{raw}) \approx x \\ y_{bpm}^{2D} = \sum_{i,j=0}^{p,q} (c_{ij} y_{raw}^i x_{raw}^j) = Q_{pq}(y_{raw}, x_{raw}) \approx y \end{cases} \quad (20)$$

Like for the 1D case, the 2D polynomial fitting is based on a regression model, but now in 2 dimensions. For our types of inverted functions, defined by the cross-section geometry of the BPM pickup, a maximum order of  $p, q \leq 5$  usually gives sufficient good results – typically  $\chi^2 \rightarrow 1$  and the RMS error  $< 10^{-2}$  – and was used for all corrections studied for the HSR BPMs. Again, due to the symmetry only the odd coefficients in Eq. (20) are used, however, this is not true for the *cross-term* coefficients  $p \neq q$ .

Evidently, this 2D correction works best if the two  $\Delta/\Sigma$  axis, i.e. the BPM pickup electrodes, are arranged along the horizontal  $x$  and vertical  $y$  axis. This is true for the HSR orthogonal BPM button arrangement, but not for the  $30^\circ$  HSR corner BPM buttons, still the 2D polynomials can achieve a sufficient correction for the non-orthogonal case.

## B. Results

The polynomial correction utilizes the  $\Delta/\Sigma$  data from the electrostatic numerical analysis, acquired and post-processed on a 0.5 mm  $xy$  grid, as shown in Section III C, and was performed within the same *Mathematica* script. With  $f$  and  $g$  being present as numerical functions it is particularly simple to invert them by a *transpose* operation, truncate the range as reasonable, and then interpolate the resulting  $f^{-1}$  and  $g^{-1}$  data for the following 1D or 2D polynomial fit.

A 1D polynomial correction for the HSR BPMs was studied only for “educational” purposes and should not be considered. With  $p = 5$  and due to the symmetry it requires only 3 coefficients:

$$U_p(x) = c_1x + c_3x^3 + c_1x \quad (21)$$

and was applied in the range  $-0.96 < f^{-1}(x_{raw}) < 0.96$ .

For all practical cases in the HSR, the 2D polynomial correction is considered. For this study we limited the polynomial order to  $p = 5, q = 4$ , which may need to be revisited for some cases. This would lead to a  $25 \times 25$  matrix for the polynomial coefficients, but due to the symmetry, many coefficients are zero or turn out to have negligible small values.

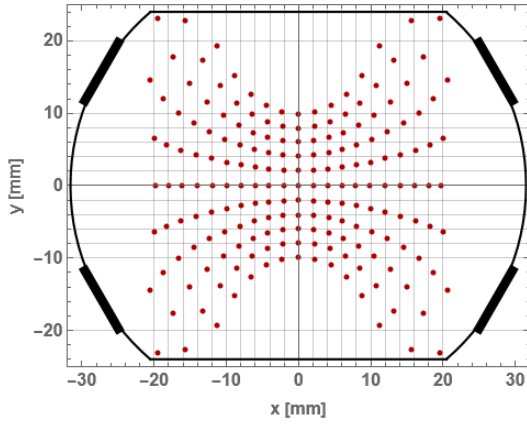
Except for the “trick” BPM case, we need 9 coefficients per axis:

$$\begin{aligned}
Q_{54}(x, y) = & c_{10}x^5 + c_{30}x^3 + c_{50}x^5 \\
& c_{12}xy^2 + c_{32}x^3y_2 + c_{52}x^5y^2 \\
& c_{14}xy^4 + c_{34}x^3y^4 + c_{54}x^5y^4
\end{aligned} \tag{22}$$

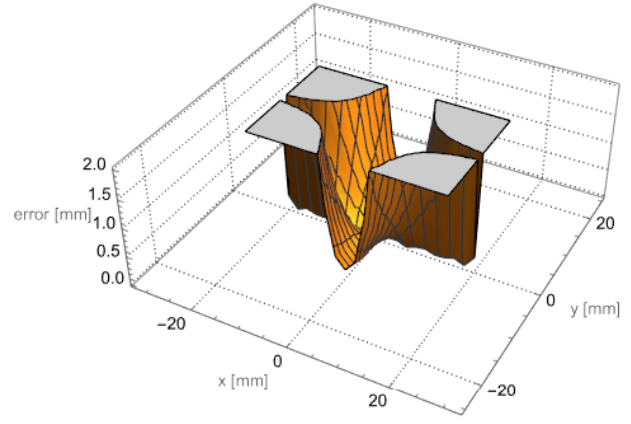
$$\begin{aligned}
Q_{54}(y, x) = & c_{10}y^5 + c_{30}y^3 + c_{50}y^5 \\
& c_{12}yx^2 + c_{32}y^3x_2 + c_{52}y^5x^2 \\
& c_{14}yx^4 + c_{34}y^3x^4 + c_{54}y^5x^4
\end{aligned} \tag{23}$$

A “reasonable” fitting range is important, a too small range leads to large errors towards the corners of the  $xy$  plane of interest, a too large range results in large errors everywhere. As indicated, e.g. in Fig. 9a, the operational range of the HSR arc BPMs foreseen is  $-23 < x < 23$  mm,  $-3 < y < 3$  mm, therefore we looked for a larger horizontal fit range, like  $-0.85 < f^{-1} < 0.85$ , while keeping the vertical fit range smaller, typically  $-0.5 < g^{-1} < 0.5$ . These fit range values may have to be revisited on the individual case.

Figures 15 to 17 summarizes the polynomial correction for the corner and orthogonal BPM, as well as for the “trick” with 3 electrodes for the corner BPM for beam with large horizontal offset. On the left side the correction performance is visualized as points (dots), placed in the area  $\pm 20 \times \pm 10$  mm for nominal  $2 \times 2$  mm position steps, indicated as line graticule. The better the dots match on the grid of the graticule, the lower is the error between the *true* and the *measured*, i.e. the corrected beam position  $(x_{bpm}, y_{bpm}) - (x, y)$ . The error is shown as absolute value (modulus) on the right side graphs for a range  $0 \dots 2$  mm.



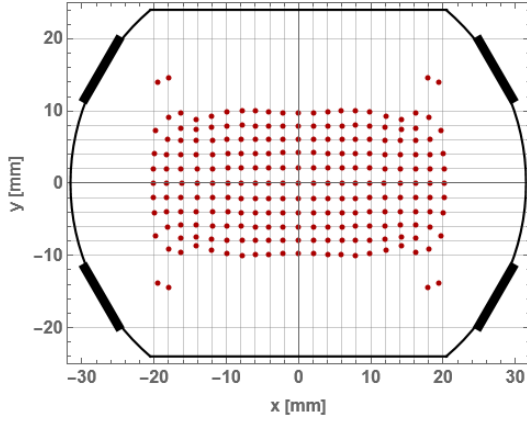
a 1D polynomial fit correction



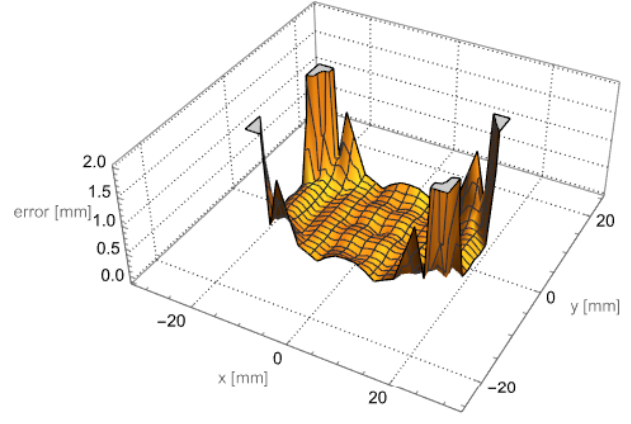
b Absolute error  $|(x_{bpm}^{1D}, y_{bpm}^{1D}) - (x, y)|$

$$c_1^x = 15.6025, \quad c_3^x = -0.502556, \quad c_5^x = 14.7967$$

$$c_1^y = 33.0943, \quad c_3^y = -13.8763, \quad c_5^y = 389.408$$



c 2D polynomial fit correction.



d Absolute error  $|(x_{bpm}^{2D}, y_{bpm}^{2D}) - (x, y)|$

$$c_{10}^x = 15.9371, \quad c_{30}^x = -3.1729, \quad c_{50}^x = 18.6844,$$

$$c_{12}^x = -18.1285, \quad c_{32}^x = 28.7611, \quad c_{52}^x = -20.8357,$$

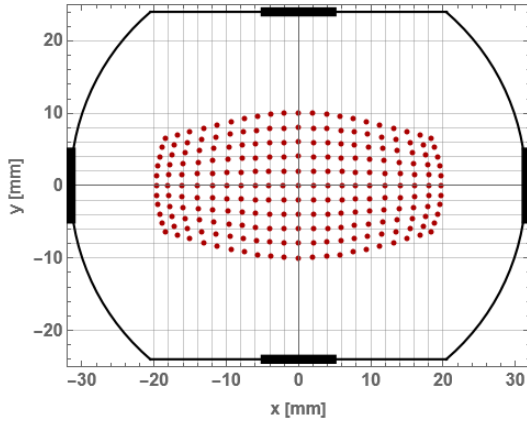
$$c_{14}^x = 7.65207, \quad c_{34}^x = -42.9883, \quad c_{54}^x = 36.5936$$

$$c_{10}^y = 34.2644, \quad c_{30}^y = -45.4929, \quad c_{50}^y = 16.8735,$$

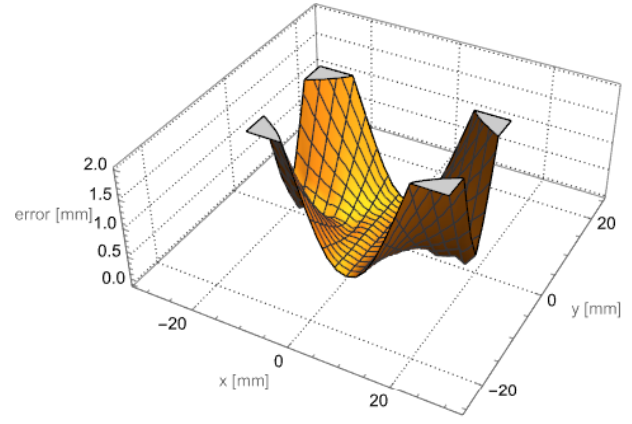
$$c_{12}^y = -49.5561, \quad c_{32}^y = 249.601, \quad c_{52}^y = -232.271,$$

$$c_{14}^y = 567.256, \quad c_{34}^y = -2020.13, \quad c_{54}^y = 1736.78$$

Figure 15. Polynomial fits for the HSR corner BPM.



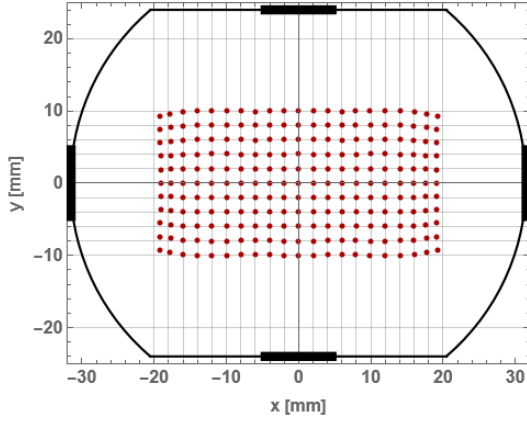
a 1D polynomial fit correction.



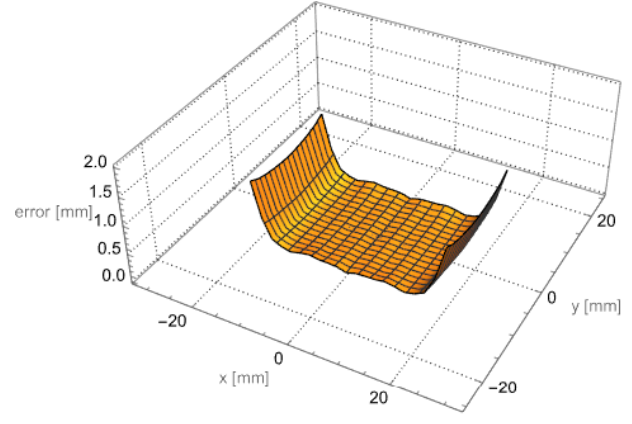
b Absolute error  $|(x_{bpm}^{1D}, y_{bpm}^{1D}) - (x, y)|$

$$c_1^x = 14.2871, \quad c_3^x = -1.34726, \quad c_5^x = 11.1694$$

$$c_1^y = 14.1461, \quad c_3^y = 2.14885, \quad c_5^y = 4.49846$$



c 2D polynomial fit correction.



d Absolute error  $|(x_{bpm}^{2D}, y_{bpm}^{2D}) - (x, y)|$

$$c_{10}^x = 13.8174, \quad c_{30}^x = 1.7459, \quad c_{50}^x = 7.27535,$$

$$c_{12}^x = 1.75408, \quad c_{32}^x = -0.730107, \quad c_{52}^x = 5.83343,$$

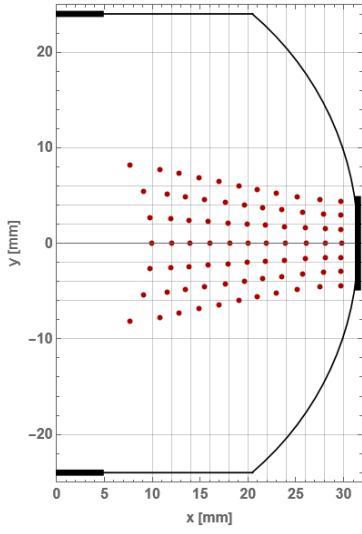
$$c_{14}^x = 2.20115, \quad c_{34}^x = -19.3716, \quad c_{54}^x = 40.5884$$

$$c_{10}^y = 14.0504, \quad c_{30}^y = 2.29542, \quad c_{50}^y = 4.82214,$$

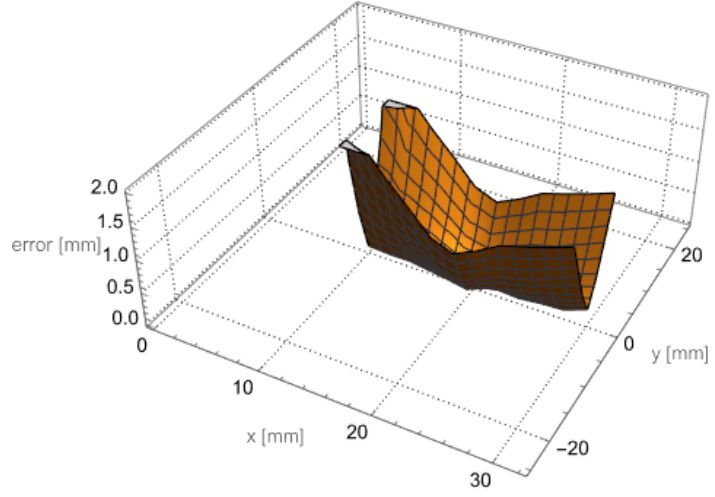
$$c_{12}^y = 3.53551, \quad c_{32}^y = -0.25992, \quad c_{52}^y = 7.33069,$$

$$c_{14}^y = 1.89072, \quad c_{34}^y = -3.48808, \quad c_{54}^y = 20.135$$

Figure 16. Polynomial fits for the HSR orthogonal BPM.



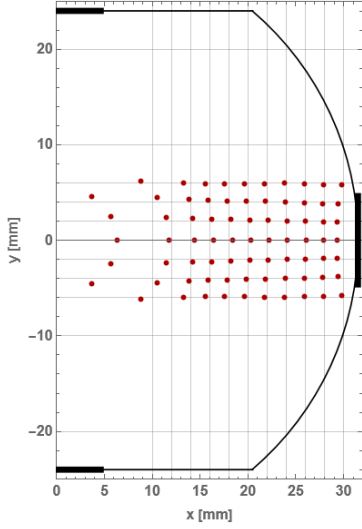
a 1D polynomial fit correction.



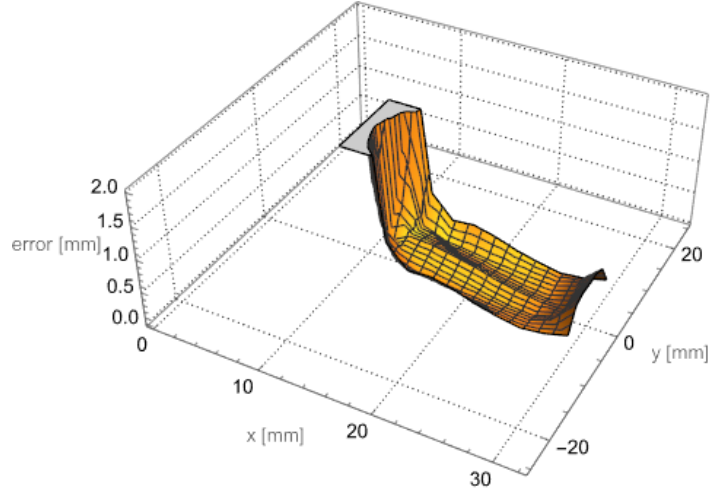
b Absolute error  $|(x_{bpm}^{1D}, y_{bpm}^{1D}) - (x, y)|$

$$c_0^x = 7.87524, \quad c_1^x = 33.2209, \quad c_2^x = -103.633, \quad c_3^x = 265.939, \quad c_4^x = -308.582, \quad c_5^x = 135.947$$

$$c_1^y = 21.0226, \quad c_3^y = 7.7476, \quad c_5^y = 9.28555$$



c 2D polynomial fit correction.



d Absolute error  $|(x_{bpm}^{2D}, y_{bpm}^{2D}) - (x, y)|$

$$c_{10}^x = 104.863, \quad c_{20}^x = -331.279, \quad c_{30}^x = 599.922, \quad c_{40}^x = -535.182, \quad c_{50}^x = 191.929,$$

$$c_{12}^x = 55.3974, \quad c_{22}^x = 317.144, \quad c_{32}^x = -903.172, \quad c_{42}^x = 1119.75, \quad c_{52}^x = -478.12,$$

$$c_{14}^x = 283.699, \quad c_{24}^x = -305.59, \quad c_{34}^x = -131.092, \quad c_{44}^x = 1093.72, \quad c_{54}^x = -704.419$$

$$c_{10}^y = 20.2339, \quad c_{30}^y = -36.5747, \quad c_{50}^y = 113.052,$$

$$c_{12}^y = 3.83639, \quad c_{32}^y = -15.4246, \quad c_{52}^y = 386.274,$$

$$c_{14}^y = 2.85023, \quad c_{34}^y = 81.0456, \quad c_{54}^y = -167.443$$

Figure 17. Polynomial fits for the horizontal HSR orthogonal “trick” BPM.



As mentioned, the results for the 1D polynomial corrections are included for illustration purposes only, for all practical applications of the BPMs in the HSR only the 2D polynomial corrections should be used!

Finally, below the graphical results, are listed all the calculated polynomial coefficients  $c_{ij}^{x,y}$ .

Comparing the results of the orthogonal and the corner BPM, for both button arrangements the errors of the non-linear position corrections are acceptable, for the operational range of the HSR well below 0.5 mm. However, comparing Fig. 15d and Fig. 16d still shows the errors of the orthogonal button arrangement being lower, and a better regression performance that is also reflected by the lower values of the higher-order polynomial coefficients. The orthogonal button arrangement has the intrinsic advantage to the corner BPM that we are already measuring in the horizontal and vertical plane, plus the fact of the orthogonality.

### C. Implementation

The polynomial correction should be implemented after all decimation and averaging algorithms, either in the FPGA firmware code or in the post-processing software. The ADC raw data of the four BPM read-out channels is processed following Eq. (12) for the corner or orthogonal button arrangement, with  $\phi_{R,L,U,D} \equiv ADC_{1,2,3,4}$  or  $\phi_{UR,DR,UL,DL} \equiv ADC_{1,2,3,4}$  being the rawADC *count* values proportional to the electrode signal voltages  $v_{elec}$ . The resulting  $\phi_{h,v} \equiv x_{raw}, y_{raw}$  values in Eq. (12) are now the *raw* normalized horizontal and vertical  $\Delta/\Sigma$  position information, ranging  $-1 < (x_{raw}, y_{raw}) < 1$ , which need to be scaled and corrected. This is simply performed by calculating  $x_{bpm}^{2D}, x_{bpm}^{2D}$  from Eq. (20), which simplifies to Eqs. (22) and (23) for both electrode arrangements – but not for the *orthogonal “trick”* – using the polynomial coefficients given below the Figs. 15c and 16c, while the orthogonal “trick” requires a few additional coefficients, as listed below Fig. 17c.

## V. ESTIMATION OF THE BPM RESOLUTION

The HSR BPM system has to cover a large variety of beam types (particle species) and formats (bunch spacing, number of bunches), as well as a large range of bunch intensities, shapes and length, starting with low bunch charges during the commissioning of the new machine, up to and beyond the designed beam intensities. Moreover, for the luminosity operation of proton beams at energies of 275 GeV or 100 GeV, the beam orbit in the HSR arcs has to be shifted from its nominal location in the center of the vacuum chamber to outside or inside, i.e. horizontally by  $\sim 20$  mm, adding another challenge. The performance of the HSR BPM system has to meet a set of well defined requirements under these various beam conditions.

The BPM precision or *resolution* is one of the key performance parameter of any BPM system, and it depends on those beam conditions, as well as on the measurement time or averaging interval. The illustrations in Fig. 18 recalls the definitions of *accuracy* and *precision* for a measurement. The accuracy, i.e. how close is the measured value to the true value, is related to the correct scaling of the BPM, and was mostly covered in the previous sections, however, ignoring the important aspect about the *BPM offset*, which is mostly related to the alignment of the BPM pickup and to asymmetries in the BPM read-out electronics (*electronic offset*). The measurement precision, i.e. how good can we reproduce the measurement, and the resolution, i.e. what is the smallest difference our measurement can detect, are related to each other, basically on different times scales. Temperature drifts, aging effect, etc., effect the measurement precision, thermal noise, power supply ripple, electro-magnetic interferences (EMI), quantization errors of ADCs, clock jitter, etc., limit the resolution of a beam position measurement.

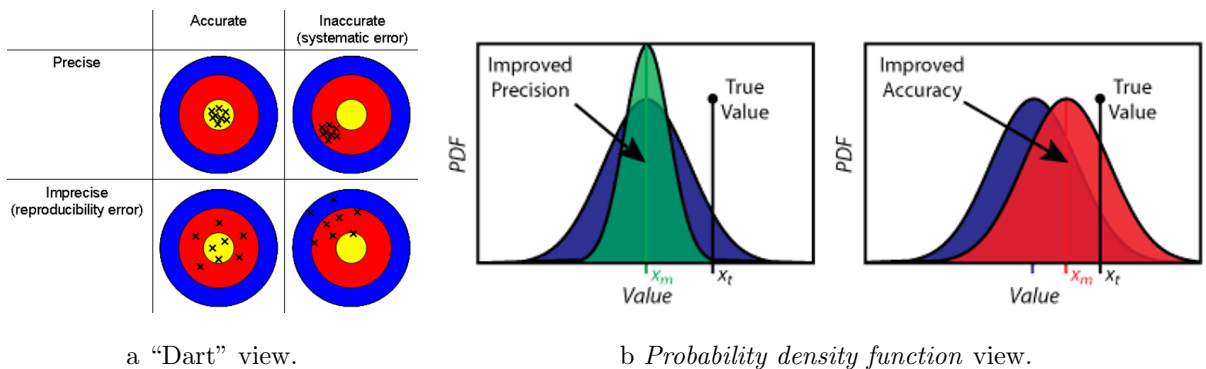


Figure 18. Accuracy and precision terminology for a measurement.



## A. BPM signal processing

The achievable resolution of a BPM is related to several factors:

- The *position sensitivity* of the BPM pickup,  $d(\Delta/\Sigma)_{x,y}/dx, y$ , which is the gradient of the normalized position  $\Delta/\Sigma$  characteristic, as discussed in Section III. Figures 9c, 9f, 10c and 10f shows the position sensitivity for the corner and orthogonal BPM button configurations, for horizontal and vertical axis, and Fig. 11c for the horizontal “trick” of the orthogonal configuration for large horizontal beam displacements. Usually this sensitivity gradient is given for a beam near the center of the BPM,  $x, y \approx 0$ , however, for the HSR BPM operating at 275 GeV and 100 GeV beam energies with a large horizontal displacement for the proton beam, the value at  $x = \pm 20$  mm is of particular interest (see also Fig. 12c).

- The *thermal noise* added to the BPM button signals by all resistive or lossy elements in the read-out signal processing electronics. This voltage of this noise is given by

$$v_{noise,RMS} = \sqrt{4k_B T R \Delta f} \quad (24)$$

with  $k_b = 1.38 \times 10^{-23}$  J/K being the *Boltzmann* constant,  $T$  the operating temperature in K,  $R$  the value of the resistor or resistive element in  $\Omega$  and  $\Delta f$  the operating bandwidth of the read-out electronics.

- The *added* thermal noise by active gain stages (amplifiers), usually specified by their *noise factor* or *noise figure*.
- The *quantization noise* or *quantization error* given by the finite quantization of the ADCs, when converting the analog waveform of the BPM button signals into a digital, i.e. numerical value.
- The *clock jitter* of the ADC sampling clock signal, which should sample the analog waveform in equidistant time intervals, which are then distorted, resulting in additional uncertainty of the converted BPM signal waveform.
- *Environmental aspects*, like electro-magnetic interference (EMI) to the signal cables or read-out electronics from high pulsed power systems in close proximity (RF

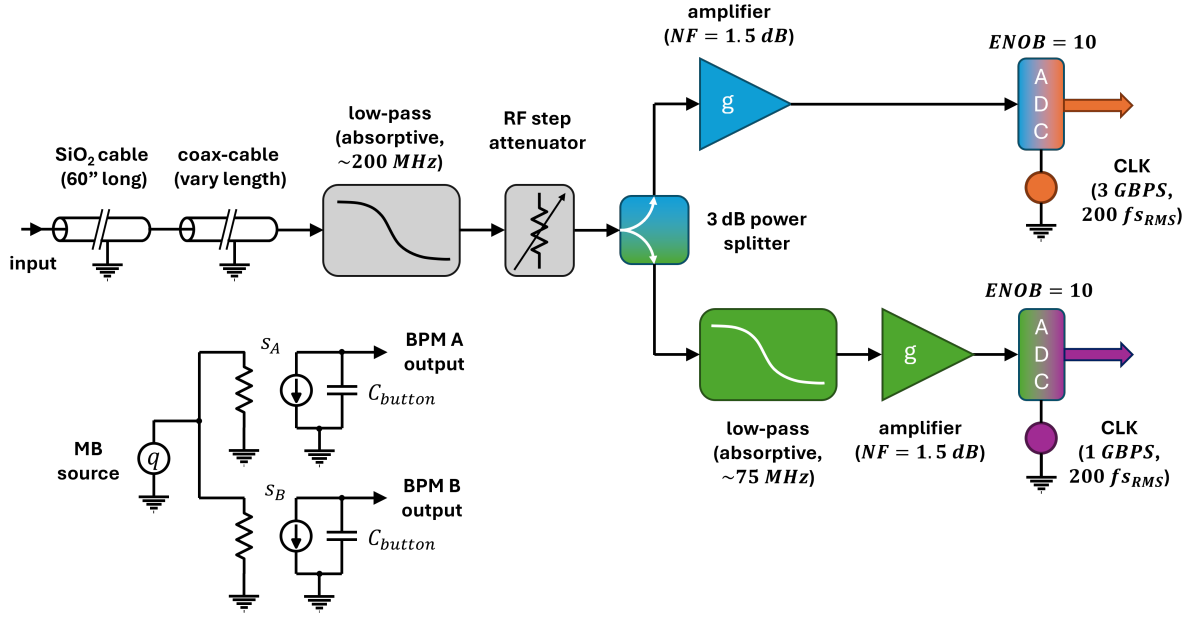
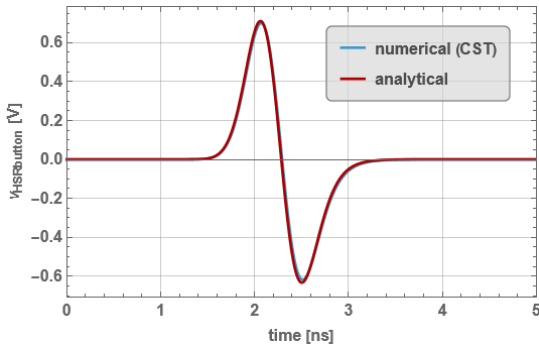


Figure 19. Signal processing scheme, 1-of-2 channels, of the HSR BPM read-out analysis.

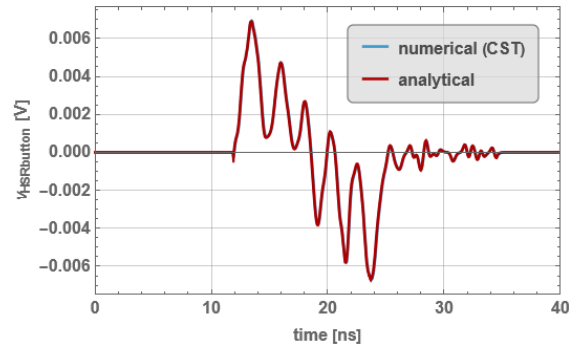
systems, kicker, septa, switched power supplies, etc.) adding an unwanted contents to the BPM signals or *ground loops* and other grounding issues, leading to an uncontrolled signal reference.

While it maybe possible to estimate the achievable BPM resolution analytically from the closed-form equations of the BPM sensitivity, thermal noise and ADC quantization error, there are many details that complicate the picture and may lead to a wrong result. For the HSR BPM we therefore use a brute-force numerical approach, basically a numerical analysis of the entire BPM signal processing chain, including the ADC. Figure 19 shows a simplified block diagram of 1-of-2 BPM channels, as it was implemented in the *Keysight Pathwave Advanced Design System (ADS)*, see also the overview schematic Fig. 1. Here we utilize the *ADS transient solver* to numerically analyze a simplified model of the BPM read-out electronics in the time-domain, using the BPM button electrode output signal waveform as stimulus.

A multi-bunch **MB source**, shown in the lower-left corner of Fig. 19, uses the waveform generated by a numerical EM analysis of the HSR corner BPM using the *CST Studio wakefield solver* or by applying the analytical analysis, e.g. based on Eqs. (1) to (3). In practice, numerical and analytical results are basically identically, see Fig. 20, with the analytical analysis getting the result much faster. The button electrode output signal waveforms are always referenced to a bunch charge of  $q_{bunch} = 1 \text{ nC}$  for the beam traveling



a *Gaussian* bunch,  $\sigma = 60$  mm.



b RHIC bunch, PP-Rebuckt02-17Aug24.

Figure 20. Output signal waveform of a HSR corner button to a centered bunch of  $q_{bunch} = 1$  nC.

through the center of the corner BPM pickup,  $x = y = 0$  mm. The `MB source` in *ADS* allows the concatenation of this single bunch waveform into a bunch train, as well as into batches of bunch trains with a given gap, in this way we are able to simulate some of the beam formats used in the HSR. The bunch intensity is scaled to the charge value of interest, indicated by the  $q$  symbol in the `MB source`.

To correctly model the *equivalent circuit* (see lower-left in Fig. 19) and the transfer function Eq. (2) of the button, the button capacitance  $C_{button}$  was evaluated with help of a numerical time-domain EM analysis of the corner BPM geometry, using the time-domain  $S_{11}$  reflection coefficient  $\Gamma(t)$  provided by the *CST Studio* software. A simple graphical fit to the theoretical response

$$\Gamma(t) = \begin{cases} 0, & t < t_D \\ 1 - 2e^{-\frac{t-t_D}{\tau}}, & t > t_D \end{cases} \quad \text{with: } \tau = Z_0 C_{button} \quad (25)$$

yields the button capacitance to be  $C_{button} \approx 2.6$  pF, see Fig. 21. A delay-time  $t_D \approx 460$  ps

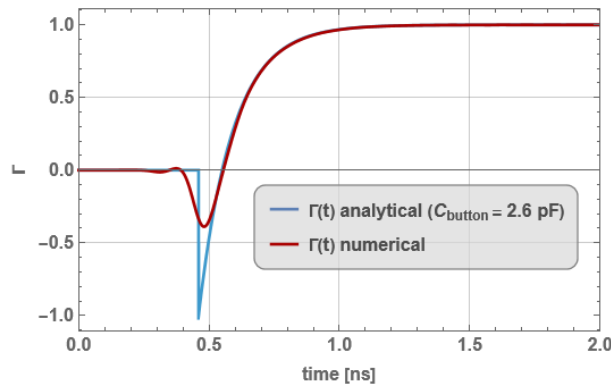


Figure 21. Determination of the button capacitance  $C_{button}$ .

in Eq. (25) accounts for the length of the transmission-line between port and button,  $Z_0 = 50 \Omega$  is the characteristic impedance of the line.

As illustrated in Fig. 19, the equivalent circuit of the HSR BPM button is modeled as voltage-controlled current source in *ADS* and includes the button capacitance  $C_{button}$ . The **MB source**, mimicking the HSR beam-to-button action, feeds two button BPM equivalent circuits, **BPM A** and **BPM B**, representing an adjacent, symmetric pair of button electrodes, e.g. the horizontal or vertical buttons of the orthogonal BPM. For a simulation of a beam in the center of the chamber,  $x = y = 0$  mm, the gain factors are set to  $s_A = s_B = 1$ , for a displaced beam,  $s_A, s_B$  are calculated according to the results of the position characteristic Section III C. Here, all bunch signal intensities are referenced to a centered beam in the corner BPM, with  $q_{bunch} = 1$  nC, therefore we scale  $\phi_{elec}(x, y)$  of the corner BPM,  $\phi_{elec}(x, y) \rightarrow \phi(x = y = 0) = 1$ , and then retrieve the  $s_A, s_B$  gain factors for a beam with an arbitrary displacement, i.e. *beam position*  $x \neq 0$  or  $y \neq 0$ . The potential differences between corner BPM and orthogonal BPM for horizontal and vertical beam positions are analyzed and known, Section III C, so it is trivial to calculate  $s_A, s_B$  also for the orthogonal BPM.

The upper part of Fig. 19 shows 1-of-2 read-out channels implemented in the *ADS* circuit simulation software, that are fed from the **BPM A** and **BPM B** outputs of the button equivalent circuits. We used a 1524 mm long sample of a  $\text{SiO}_2$ , type 141 mil coaxial cable (*Times Microwave Corp., TMS*), and characterized it with the vector-network analyzer (VNA). The S-parameter results were then fitted by a coaxial cable simulation model supplied in *ADS*, now enabling the simulation for any cable length, here extended to 60 inch as required for the BPM cables running inside the HSR arc cryostats. The same procedure was applied to  $\frac{1}{4}$  inch and  $\frac{3}{8}$  inch *Heliax* type coaxial cables, as well as for a *LMR-240* cable. A comparison of the measure sample and the technical information provided by the datasheet from industry showed good agreement when applying the fit to the *ADS* coaxial cable model. The  $\frac{3}{8}$  inch *Heliax DF2-50* is preferred for the long cable runs between BPM pickup and read-out electronics.

As of the large differences in bunch intensities, length's and shapes in the HSR, the button BPM signals cover a large dynamic range, which includes both, the bunch intensity **and** the beam position, see Eq. (1). A typical 12-bit or 14-bit analog-to-digital converter (ADC) has a usable dynamic range of  $\sim 60$  dB, which is insufficient for the *digitalization* of the HSR BPM button signals. To better cover the entire BPM signal dynamic range,

we decided to split the signal after an absorptive low-pass filter with  $\sim 200$  MHz cut-off frequency and a step-attenuator, see Fig. 19. The upper, blue colored high-frequency branch uses a low-gain amplifier ( $g \approx 0 \dots 10$  dB) and the feeds into an ADC. This branch is designed to acquire the BPM signals on a bunch-by-bunch bases when the HSR is in collision operation, i.e. the bunch spacing is  $t_{bunch} = f_{RF}/6 = 10.15 \text{ ns}$ <sup>2</sup> and the particles in the bunches have a longitudinal *Gaussian* distribution with  $\sigma = 60$  mm. The lower, green colored low-frequency branch uses a high-gain amplifier ( $g \approx 40 \dots 50$  dB) after passing through another absorptive low-pass filter with  $\sim 75$  MHz cut-off frequency. This branch acquires the BPM signals at injection energy, with long proton or ion bunches being present (up to  $\sim 7.5$  m), spaced by  $t_{bunch} = f_{RF}/24 = 40.6 \text{ ns}$ .

Despite splitting the BPM button signals into separate, simultaneously acquiring high- and low-frequency branches, the RF step-attenuator in front of the power divider, see Fig. 19, is required to optimized the signal levels at the inputs of the ADCs for the different beam/bunch parameters and also to compensated for the insertion loss variations due to the different cable length in HSR BPM system.

## B. ADS transient analysis of the HSR BPM read-out electronics

All components and subsystems shown in Fig. 19, together with a few other not shown supporting elements, have been implemented in *ADS*, using the non-linear transient solver for the analysis of this electrical network. A low-pass prototype, serving the two absorptive filters, was based on the well-known quasi-*Gaussian* absorptive ladder network and further optimized using the ADS optimizer within a dedicated S-parameter simulation. For the RF step attenuator and the 3 dB power splitter we used S-parameter models provided by industry, *ADS* then applies the convolution integral “on-the-flight” when converting the frequency-domain model data into the time-domain during the transient simulation procedure, utilizing inter- and extrapolation as necessary. For the gain-stages the internal *ADS ideal amplifier* model was used, applying the necessary gain and using a noise figure of  $NF = 1.5$  dB. The ADCs were modeled based on the data sheets provided by the industry, trying to exactly implement the recommended analog, *balun* input circuit and the ADC load impedance. The *ADS* build-in *sample & hold* and *quantizer* models were used to model the digital part of the ADCs. The sample & hold receives the clock signal

---

<sup>2</sup>  $f_{RF} = 591.1$  MHz is the highest harmonic acceleration frequency in the HSR.

from a source with 200 fs RMS jitter, the ADC of the upper, high-frequency branch is clocked with  $f_{CLK-HF} = 3 \text{ GHz} \equiv 3 \text{ GBPS}$ , the ADC in the lower, low-frequency branch with  $f_{CLK-LF} = 1 \text{ GHz} \equiv 1 \text{ GBPS}$ .

The BPM read-out channel with two ADCs as shown in Fig. 19 is implemented as sub-circuit in *ADS*. Two of them are called by the main simulation circuit that runs the transient solver, named **BPM A** and **BPM B**, along with the **MB source**. Other elements, like the absorptive low-pass filters, are implemented as sub-circuits as well, with relevant parameters, e.g. 3 dB cut-off frequency, being made available to the calling main circuit. The two button equivalent circuits, the clock sources and a few other circuit elements are implemented directly in the main simulation circuit level, also controlled by a set of parameters. The gain and attenuator settings were always kept the same for both read-out channels, also when simulating beams with large displacement. The *maximum time step* in the *ADS* transient simulation was set to  $t_{step} = t_{CLK-HF}/10 = 33.3 \text{ ps}$ , however, the software internally selects smaller time steps as necessary. The thermal noise if activated for all resistive circuit elements, the noise bandwidth was set to  $\Delta f_{noise} = 1/(2t_{step}) = 15 \text{ GHz}$ .



Please note, this is the maximum noise bandwidth which can be simulated, the actual noise bandwidth  $\Delta f$  that shows up at the ADC input following Eq. (24) is mostly defined by the bandwidth of the low-pass filters in the circuit.

Most simulation parameters, like bunch waveform, bunch-to-bunch distance, bunch charge, number of bunches per batch, total number of batches, physical length of the cables, BPM gain settings (for a specific beam displacement / position), gain and attenuator settings, clock signal frequencies and details of their waveforms, etc., can be simply modified by changing the corresponding value / file name in the main simulation circuit. The ADC output signals of the two BPM buttons, **digiA** and **digiB**, are still “analog” voltage waveforms in *ADS*, given by the internal *ADS* time step and a “voltage” level defined by the maximum quantization value. In our analysis we set the *ADS* quantizer to  $N=1024$ , which is equivalent to the *effective number of bits* (ENOB) of the ADCs chosen for this analysis. Therefore the results are ranging  $0 < \text{digiA}, \text{digiB} < 1024$ . The

quantizer (ADC) reference voltage levels are empirically set to ensure a symmetric and well balanced leveling wrt. the input waveform. For the setting of gain / attenuation in the two channels we followed the rule of thumb, the higher level signal should be in the regime of 60...70% *full-scale range* (FSR) of the ADC.

The ADC output signals `digiA` and `digiB` are saved as *ACSH* text files for further analysis. These are large files, as they are still discretized by the internal time step of 33.3ps or smaller. We added a *ADS time stamp* waveform, `vTime`, which is saved along with the two ADC output waveforms, and indicates the actual ADC clock cycles. In the post-processing this allows to synchronize and decimate the `digiA` and `digiB` “analog” waveform files to the ADC clock cycle.

### C. Results for proton bunches with a large horizontal displacement

The *resolution* of the HSR BPMs probably is most important in collision mode, and please keep in mind, the achievable resolution depends on the statistics of the measurement and on the *measurement time*, or averaging time, which is linked to the system bandwidth. We may distinguish three different use cases, having quite different time scales or bandwidth needs using the HSR beam position data:

1. A *beam orbit* measurement for analyzing the RMS orbit of all or of a particular BPM in the control room display and as input for the transverse beam *orbit feedback system* (OFB). The averaging time on the BPM data should be equal or smaller than the equivalent bandwidth required for the OFB, which typically is in the order of 1000 turns for most storage rings.
2. A *turn-by-turn* position measurement, synchronized for all BPMs in the HSR. This position measurement is typically utilized for beam optics studies, with the BPM data analyzed as the response of the machine after an excitation, e.g. by a transverse kick of an AC dipole. All BPM data within a turn should be averaged, assuming the digitized BPM signal waveforms are well separated on a turn-by-turn bases.
3. A *bunch-by-bunch* or selected *single bunch* position measurement for 1 or many turns. This type of dedicated bunch position data is typically requested during special machine studies or by the collision experiment, e.g. analyzing beam orbits or positions of colliding vs. non-colliding bunches, etc.

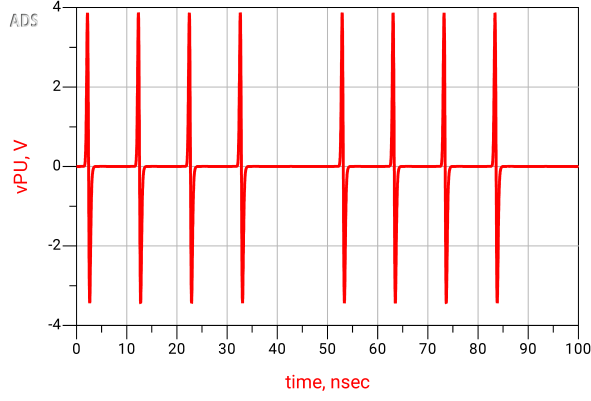


Figure 22. Proton bunch / batch signal generated by the **MB source** in *ADS*.

While we could study the resolution of the HSR BPM for all the different HSR beam types and formats, unfortunately the execution time of the *ADS* software to generate enough position data, e.g. for 1000 turns is rather long<sup>3</sup>. Therefore we limit our initial analysis for the case with a large horizontal beam displacement,  $x = +20$  mm, for 4 consecutive proton bunches,  $q_{bunch} = 5$  nC, of *Gaussian* long. distribution,  $\sigma = 60$  mm, and spaced by 10.15 ns. A 5<sup>th</sup> bunch is an *empty bucket*, so we can imagine that we simulate the BPM signal behavior for a HSR fill with 4 proton bunches for a given number of turns, see also Fig. 22.

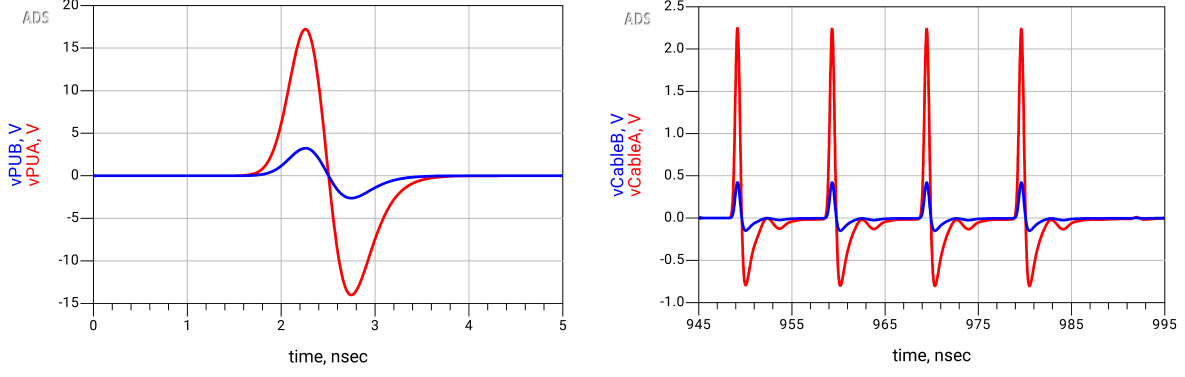
In this analysis we want to compare the resolution of the corner BPM vs. the orthogonal BPM applying the “trick” with the virtual center electrode. As our waveform is based on a 1 nC bunch from a corner BPM button, a factor  $q = 5$  has to be accounted for in the **MB source**, see Fig. 19. For the  $x = +20$  mm horizontal beam displacement the “gain” factors  $s_A$  and  $s_B$  for the two cases are referenced to a centered beam ( $x = y = 0$  mm) of

Table I. “Gain” factors for a beam with  $x = +20$  mm displacement.

	$s_A$	$s_B$
corner BPM	2.53233	0.198646
orthogonal “trick” BPM	5.30905	0.996553

<sup>3</sup> A *ADS* simulation of 4 bunches, 1024 turns and 240 meter long cables takes about 24 hours.





a At the HSR BPM pickup outputs.

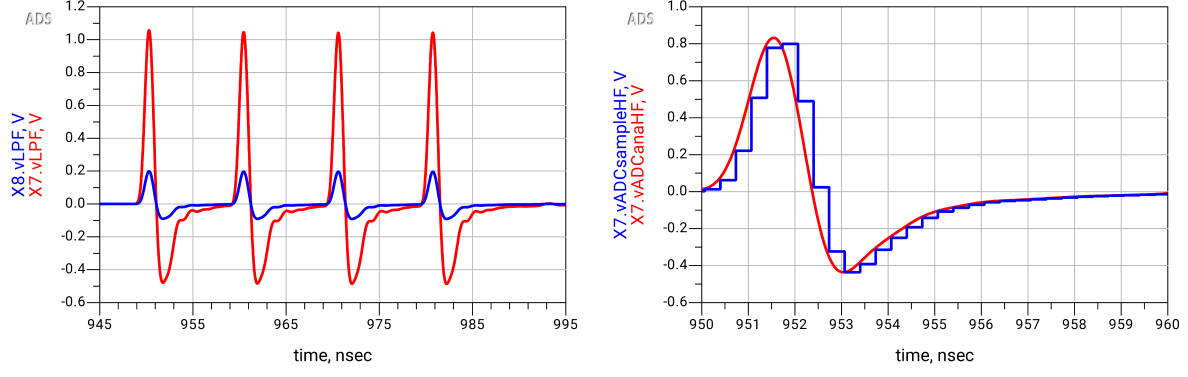
b After 240 m of  $\frac{3}{8}$  inch *Heliax* cables.

Figure 23. Bunch signal waveforms for FE channel **A** and **B**.

the corner BPM and evaluated following Section III C. We apply those factors, Table I, to  $s_A$  and  $s_B$  in the **voltage-controlled current sources** of our button equivalent circuit Fig. 19. Figure 23a illustrates the two **A** and **B** bunch signal waveforms at the buttons of the corner BPM. As we use the “trick” arrangement, these are the signals coming for a horizontal and a *vertical* BPM button of the orthogonal BPM for the 5 nC, 60 mm proton bunch with 20 mm horizontal offset. The *worst-case* situation – requiring long coaxial cables between the BPM pickup and the read-out electronics – is of greatest interest, therefore we analyzed the cases for a cable length of 130 m and 240 m. Figure 23b shows the attenuation and degradation of the bunch signals at the end of the 240 m of  $\frac{3}{8}$  inch *Heliax* cables, also indicating some unwanted reflection effects due to imperfections of the components in the simulated read-out system.

Figure 24 shows the bunch signal waveforms in the upper *high-frequency* (HF) branch of the front-end electronics, Fig. 19, Fig. 24a after the 200 MHz **absorptive low-pass filter** and Fig. 24b before and after the **sample & hold**. To achieve the anticipated 60...70% FSR levels in the **A channel** ADC, the **step attenuators** have been set to 0 dB and the **amplifier** gain to 8 dB for both channels (processing the signals for the orthogonal “trick” BPM).

As the BPM resolution analysis is based on statistics, we simulate 1024 batches of 4 proton bunches, with one empty bucket as shown in Fig. 22, and account them for 1024 turns in the HSR. The digitized output waveforms **digiA** and **digiB**, simulated by *ADS* are stored as ASCII text files along with the time stamp file for post-processing with a

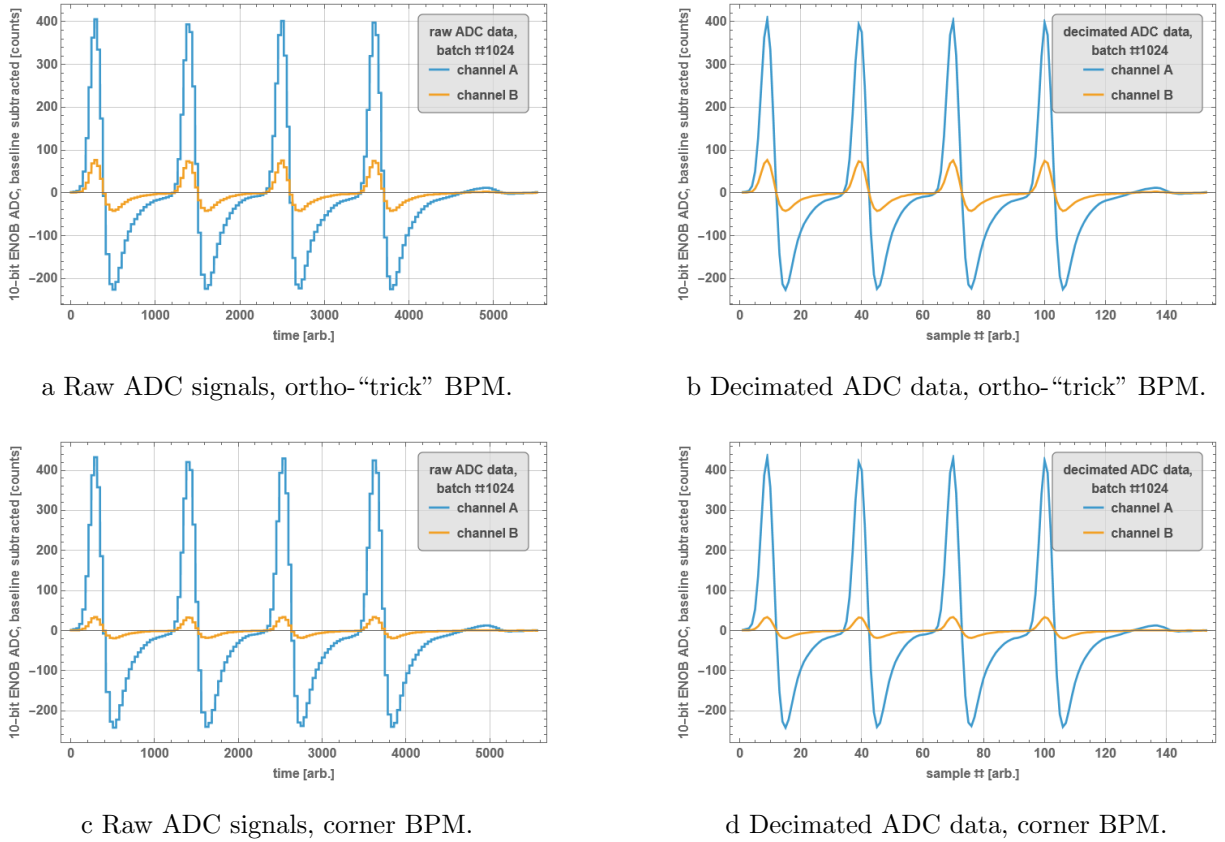


a At the 200 MHz LPF output.

b Before / after the sample & hold.

Figure 24. Bunch signals in the *HF*-branch of the FE electronics.

*Mathematica* script. The script identifies and marks the batch numbers in the raw data and subtracts the baseline from the data, therefore allows for a variety of sanity check, e.g. comparing batches and channels.



a Raw ADC signals, ortho-‘trick’ BPM.

b Decimated ADC data, ortho-‘trick’ BPM.

c Raw ADC signals, corner BPM.

d Decimated ADC data, corner BPM.

Figure 25. Bunch signals of batch #1024 in the post-processing.

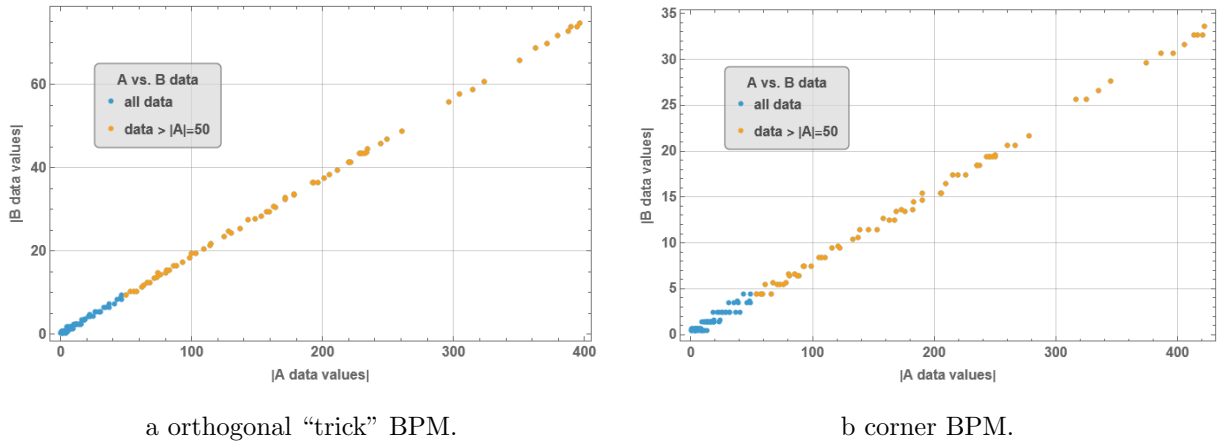


Figure 26. Decimated ADC samples of batch #1 shown as  $|digiA|$  vs.  $|digiB|$  graph.



As of the baseline subtraction, the 10-bit sample values are signed integers!

Figure 25 shows the bunch signals of the last batch (turn), batch #1024, of channel A and B in the post-processing, Figs. 25a and 25c the raw ADC data as acquired from the *ADS* and Figs. 25b and 25d the ADC data after applying the decimation with help of the time stamp data.

Each batch of 4 bunches plus an empty bucket has  $\sim 150$  ADC samples, after decimation lets simply call them  $A$  and  $B$ . Figure 26 plots the absolute values of those samples, i.e. the modulus  $|A|$ ,  $|B|$ , in a parametric form  $|A|$  vs.  $|B|$  for the orthogonal “trick” BPM (Fig. 26a) and for the corner BPM (Fig. 26b). Evidently, the points fall on a linear slope crossing zero with the gradient equal to the amplitude ratio of the acquired button signals<sup>4</sup>. For the estimation of the BPM resolution, we select a threshold value, arbitrarily set to 50 counts for the higher level signal  $A$ , and will take only values  $|A| > 50$  and their channel  $B$  counterparts into the analysis, indicated as **orange points** in Fig. 26. This will remove the low-level, more noisy parts of the data, at a sampling rate of 3 GBPS we still get  $\sim 70$  samples on the 4 consequence bunches.

For the analysis we have to follow the normalization procedure, and as we took the specific button configuration – orthogonal “trick” or corner BPM – into account by setting  $s_A$  and  $s_B$ , we simply follow

$$x_{raw} = \frac{a - b}{a + b} \quad (26)$$

<sup>4</sup> Please be aware of the different scaling in those graphs, particular the vertical  $|B|$  value axis.

to get the normalized, uncalibrated horizontal beam position. To calibrate  $x_{raw}$  in Eq. (26) we have to apply the correction discussed in Section IV B, here for simplicity we use the 1D polynomial correction Eq. (17) with the 1D coefficients given in Fig. 17 for the orthogonal “trick”, and in Fig. 15 for the corner BPM configuration.

As BPM resolution we define the *standard deviation*

$$\sigma = \sqrt{\frac{1}{N} \sum_{i=1}^N (x_i - \mu)^2} \quad (27)$$

on a set of  $N$  calibrated BPM position values, while the *mean* value

$$\mu = \frac{1}{N} \sum_{i=1}^N x_i \quad (28)$$

returns the actual beam position, which was set to  $x = +20.00$  mm.

#### 1. Single batch (turn) measurement resolution

For this estimation we use the  $\sim 70$  samples on 4 consequence bunches of a single batch, equivalent to a single turn, from the two electrodes. For  $a$  and  $b$  in Eq. (26) we use the **orange sample points** of  $|A|$  and  $|B|$  shown in Fig. 26 of a given batch, here we arbitrary select batch #500. Table II lists the statistics for the corner and the orthogonal “trick” BPM configurations for the normalized, corrected (1D polynomial) position values, indicating a BPM resolution of 0.3 mm, resp. 0.08 mm for a beam with  $x = +20.00$  mm horizontal displacement, with the 3 GBPS, 10 ENOB ADC read-out electronics connected via 240 m long  $\frac{3}{8}$  inch *Heliax* coaxial cables.

Table II. Statistics of a single batch (#500).

	$\mu$ [mm]	$\sigma$ [mm]
corner BPM	19.8	0.3
orthogonal “trick” BPM	20.0	0.08



Please note, in practice the mean value  $\mu$  for the corner BPM will be improved by applying the 2D polynomial correction. Also please notice, there is some spread on the  $\sigma$ -values wrt. the selected batch #, in particular for the corner BPM, due to the rather low statistics.

## 2. Multi batch (turn), orbit measurement resolution

In practice, the ADC samples will not be processed individually as done in the previous Section V C 1, purely for the illustration of the single batch performance. Instead, we calculate the *root mean square* (RMS) value of the samples on a batch-by-batch (turn-by-turn) bases:

$$A_{\#}^{RMS} = \sqrt{\frac{1}{N} \sum_{i=1}^N A_{i,\#}^2}, \quad B_{\#}^{RMS} = \sqrt{\frac{1}{N} \sum_{i=1}^N B_{i,\#}^2} \quad (29)$$

with  $A_i$  and  $B_i$  being the  $\sim 70$  ADC samples of larger value ( $|A| > 50$ ) of the four consequence bunches of a given batch number (#). Equation (29) represents the *signal power* for each batch, measured at the two BPM buttons.



This signal power measurement assumes we are respecting the *Nyquist-Shannon* sampling theorem, the *total* signal bandwidth is half the sampling rate:  $B < f_s/2$ .

Applying the normalization Eq. (26) on the batch-by-batch calculated RMS values, Eq. (29) and calibrated those using the appropriate polynomial correction – again, here for simplicity the 1D polynomials – results in batch-by-batch, or turn-by-turn beam position values. Table III summarizes the results, again, for the 3 GBPS, 10 ENOB ADC, 240 m long  $\frac{3}{8}$  inch *Heliax* cable case. The *number of batches (turns)* rows show the statistical values for the first 10, 20, ... 1000 batches for the two BPM button arrangements. The mean values, i.e. the calibrated beam positions, are almost identically, with a larger error for the corner BPM due to the insufficient 1D polynomial correction, as expected. The standard deviation  $\sigma$  in Table III could be viewed as the *theoretically achievable position resolution* for the two BPM button configurations.

Our simulation results do not follow the simple  $\sigma \propto 1/\sqrt{n}$  characteristic, i.e. more samples equal better resolution. For the corner BPM, averaging only a small number of

Table III. Statistics on multiple batches (turns).

number of batches (turns)	corner BPM		ortho-“trick” BPM	
	$\mu$ [mm]	$\sigma$ [ $\mu\text{m}$ ]	$\mu$ [mm]	$\sigma$ [ $\mu\text{m}$ ]
10	19.8	(16.0)	20.0	8.0
20	19.8	(18.0)	20.0	6.5
50	19.8	(19.2)	20.0	5.4
100	19.8	(19.7)	20.0	4.9
200	19.8	21.2	20.0	4.8
500	19.8	20.2	20.0	4.8
1000	19.8	19.5	20.0	4.8

batches,  $\lesssim 200$  seems to have too low statistics to give a reliable standard deviation. Those  $\sigma$ -values shown in brackets in Table III vary substantially if, e.g. other batches are selected. The standard deviation results for the orthogonal “trick” BPM button arrangement looks a bit more consistent, however, averaging more then 200 batches (or turns) does not further improve the achievable BPM resolution. The reason for this resolution limit maybe linked to the finite ADC quantization, but would need more studies to verify this speculation.



The standard deviations  $\sigma$  for a single batch (turn) or for many ( $> 500$ ) batches (turns) listed in Tables II and III can be interpreted as the *best* achievable beam position resolution for a single turn, resp. multi-turn position measurement. However, despite an accurate analysis, there are several unknown factors, like EMI or ground-loops, which may degrade the BPM performance, therefore the values,  $\sim 0.3$  mm and  $\sim 80$   $\mu\text{m}$  for a single batch (turn) or  $\sim 20$   $\mu\text{m}$  and  $\sim 5$   $\mu\text{m}$  for a 1000 turn average, for the corner, resp. orthogonal “trick” BPM button configurations have to be taken with great care, and may not be achievable in practice!

## VI. BEAM-INDUCED POWER LOSSES

The HSR BPM pickups will be located between the RHIC superconducting (SC) quadrupole and dipole magnets, inside the SC-cryostat. The BPM pickup is passive cooled, through thermal conduction to the attached components, e.g. the beam pipe and screen, the bellow, the signal cables, etc. The temperature of the BPM pickup, i.e. of all the individual components like BPM body, feedthroughs, buttons, etc., will reach a state of thermal equilibrium depending on this thermal conduction and the thermal losses, and will be discussed in the following section. *Beam-induced power losses* play a major role in this thermal equilibrium, in particular for the case of high intensity proton beams with large horizontal offset. The power-loss results summarized at the end of this discussion are used as input for the estimation of the maximum temperatures we can expect in the different parts of the BPM pickup during luminosity operation at 275 GeV or 100 GeV beam energy.

### A. Theoretical background

The electromagnetic field of a charged particle, point charge, traveling with relativistic velocity,  $\beta \approx 1$ , in a metallic, perfectly conducting beam pipe has no longitudinal components, it's EM-field configuration is called *TEM* (transverse electro-magnetic). Any change in the beam pipe aperture causes a change of the EM-field, i.e. it will generate longitudinal field components which may act on a following charged particle. In this case a *Lorentz* force acts on the test charge  $q_2$ , generated by the *wake fields* of the probe charge  $q_1$ :

$$\vec{F} = \frac{d\vec{p}}{dt} = q_2(\vec{E} + c\vec{e}_z \times \vec{B}) \quad (30)$$

with  $c\vec{e}_z = \beta v\vec{e}_z$  indicating the relativistic motion of the charge in the  $z$ -direction of the beam pipe. The *wake function* of the “perturbed” beam pipe geometry, e.g. a simple discontinuity in form of a bellow, or an accelerating cavity, or a BPM pickup, etc., due to the probe charge  $q_1$  is then defined as:

$$\vec{w}(\textcolor{red}{x}_1, \textcolor{red}{y}_1, \textcolor{blue}{x}_2, \textcolor{blue}{y}_2, \textcolor{green}{s}) = \frac{1}{\textcolor{red}{q}_1} \int_{-\infty \text{ (or } 0)}^{+\infty \text{ (or } L)} dz \left[ \vec{E}(\textcolor{blue}{x}_2, \textcolor{blue}{y}_2, z, t) + c\vec{e}_z \times \vec{B}(\textcolor{blue}{x}_2, \textcolor{blue}{y}_2, z, t) \right]_{t=(\textcolor{green}{s}+z/c)} \quad (31)$$

which causes a change of the momentum on the test charge  $q_2$

$$\Delta p = \frac{\textcolor{red}{q}_1 \textcolor{blue}{q}_2}{c} \vec{w}(\textcolor{green}{s})$$

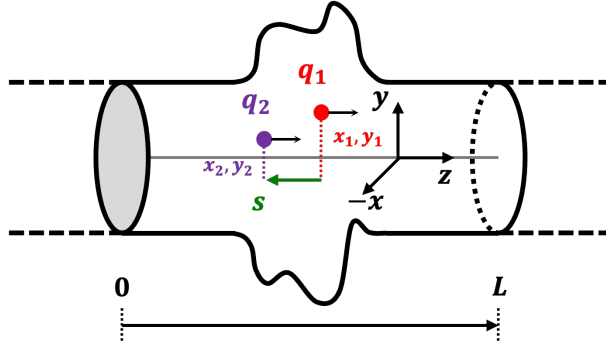


Figure 27. Two-particle model illustrating the wake function.

Figure 27 illustrates Eq. (31), for all practical cases the integration range spans the range 0-to- $L$  of the object, which needs to include fringe and decaying fields until all stored energy in the structure is completely decayed <sup>5</sup>.

For a distributed source, e.g. a beam bunch with many charged particles

$$\rho_d(\vec{r}, t) = \overbrace{\eta(x_1 - \bar{x}_1, y_1 - \bar{y}_1)}^{\text{transverse distribution}} \underbrace{\lambda(z - ct)}_{\substack{\text{longitudinal} \\ \text{distribution} \\ \text{(line charge)}}$$

the *wake potential*

$$\vec{W}_d(\bar{x}_1, \bar{y}_1, x_2, y_2, s) = \int \vec{w}(x_1, y_1, x_2, y_2, s) \eta((x_1 - \bar{x}_1, y_1 - \bar{y}_1) \frac{\lambda(z_1)}{q_1} dx_1 dy_1 dz \quad (32)$$

is derived from the wake function Eq. (31).



Please note, the point charge has an infinite frequency spectrum, the spectrum of the distributed source is limited.

The wake function of potential can be separated into longitudinal and transverse components, which are related to each other described by the *Panofsky-Wenzel* theorem. For the analysis of beam pickups, including this HSR BPM pickup, the *longitudinal* wake potential is of primary interest:

$$W_{\parallel}(s) = \int_{-\infty}^{+\infty} d\acute{s} w_{\parallel}(\acute{s}) \lambda(s - \acute{s}) \quad (33)$$

with the longitudinal wake function given as:

$$w_{\parallel}(s) = \frac{1}{q_1} \int_{-\infty}^{+\infty} dz E_z[x_2, y_2, z, (s + z)/c]$$

<sup>5</sup> This often is not achievable by numerical simulations and a reasonable threshold, i.e. a *cut* in term of wavelength  $L$  to be calculated has to be made.



In many cases we can assume the bunch source distribution as *Gaussian*:

$$\rho(\vec{r}, t) = q_1 \delta(x) \delta(y) \lambda(z - ct), \quad \text{with: } \lambda(s) = \frac{1}{\sigma \sqrt{2\pi}} \exp\left(-\frac{s^2}{2\sigma^2}\right) \quad (34)$$



Numerical simulation tools, like the wakefield solver of the *CST Studio* software used here, calculate the wake potential for a distributed source, typically a line-charge with *Gaussian* distribution.

The bunch shape dependent *total loss parameter* describes the energy loss of the bunch

$$\Delta E_{bunch} = q_{bunch}^2 k_{tot} \quad (35)$$

due to the wake fields for a line-charge distribution with negligible transverse dimensions:

$$k_{tot} = - \int_{-\infty}^{+\infty} ds W_{\parallel}(s) \lambda(s) \quad (36)$$

Finally, the *longitudinal coupling impedance* is of interest, which is defined as the frequency-domain representation of the longitudinal wake potential:

$$Z_{\parallel}(\omega) = \frac{1}{c} \int_{-\infty}^{+\infty} ds w_{\parallel}(s) e^{-j\omega s/c} \quad (37)$$

Electromagnetic software codes, like *ECHO*, *GdfidL*, *A3P*, *CST Studio* usually solve the problem numerically in the time-domain for a given geometry (and materials) and for a given bunch charge distribution, intensity and velocity (usually  $v = c$ ). Among many other parameters they return the total loss factor  $k_{tot}$ , Eq. (36), and the longitudinal coupling impedance  $Z_{\parallel}(\omega)$ , Eq. (37). The total, geometry related *power loss* in a ring accelerator can be estimated as:

$$P_{loss} = \frac{\Delta E_{bunch}}{t_{rev}} N_{bunch} \quad (38)$$

with  $t_{rev}$  being the revolution time of the machine and assuming it is filled with a number  $N_{bunch}$  of bunches of identical parameters. Alternatively, the power losses can also be calculated from the real part of the longitudinal coupling impedance:

$$P_{loss} = I_{beam}^2 Z_{loss} \quad (39)$$

with  $I_{beam} = N_{bunch} I_{bunch}$ ,  $I_{bunch} = q_{bunch} f_{rev}$ ,  $f_{rev} = 2\pi\omega_{rev} = 1/t_{rev}$  and

$$Z_{loss} = \sum_{p=-\infty}^{+\infty} |\Lambda(p\omega_{rev})|^2 \text{Re}[Z_{\parallel}(p\omega_{rev})] \quad (40)$$

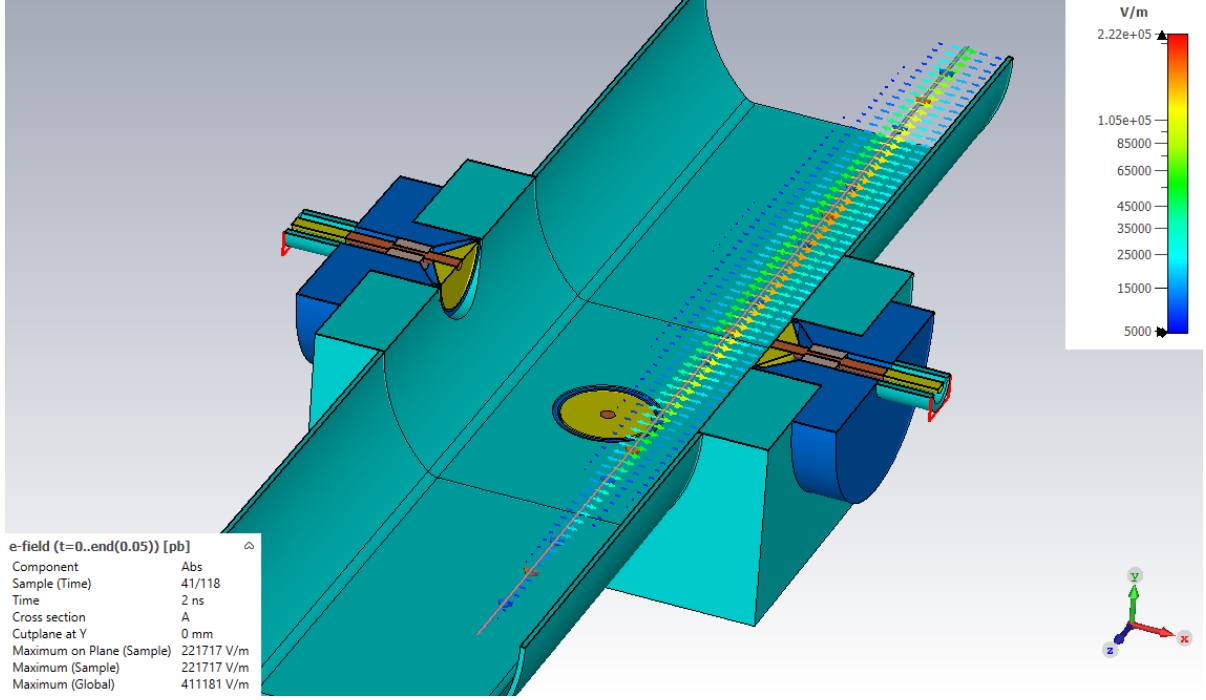


Figure 28. Electric beam field components in the xz-plane of the HSR orthogonal BPM.

by examining  $\Lambda^2 Z_{\parallel}$  at the  $p\omega_{rev}$  revolution harmonics, with  $\Lambda(\omega)$  being the normalized beam spectrum. Assuming identical bunches in the ring, which do not couple to each other, the total power loss can be calculated from the normalized *single bunch spectrum* (SBS)  $\lambda(\omega)$ :

$$P_{lossSBS} = I_{bunch}^2 N_{bunch} Z_{lossSBS} \quad (41)$$

with:

$$Z_{lossSBS} = 2N_{bunch} \sum_{p=0}^{+\infty} |\lambda(p\omega_{rev})|^2 \text{Re}[Z_{\parallel}(p\omega_{rev})] \quad (42)$$

The power losses due to beam induced wakefields, calculated by Eqs. (38), (39) and (41), are the *total power losses* due to the geometric structure of the vacuum device, caused by the energy loss in the beam bunches, Eq. (35). They include, e.g. for a beam pickup, the output signal power from the electrodes and do not elaborate where the power is dissipated. Figure 28 illustrates the electric components of the beam field, in the xz-plane, for a passing proton bunch, i.e. a *Gaussian* line charge distribution,  $\sigma = 60$  mm.



The total power losses calculated based on the loss factor, Eq. (36), are related to the geometry of the vacuum device, here the HSR BPM pickup, causing an energy loss of the beam bunch, Eq. (35), and appear also if no power dissipation is specified, e.g. *perfect electrical conductors* (PEC) are used as materials in the numerical analysis!

To analyze the *power dissipation* generated by the geometric wake field losses, e.g. how much power is dissipated in the various materials of the BPM pickup, we have to take not only the exact BPM pickup geometry, but also the electric material properties, in particular the *electric conductivity*  $\sigma$  at the operating temperature  $T$ , into account. The *CST Studio* software allows to monitor the magnetic beam field components and the related *surface currents* vs. time, and generates lists of power losses sorted by the specified materials and/or geometric components, e.g. the different parts of the BPM pickup. Figure 29 visualizes the surface currents generated by a passing proton bunch with large horizontal displacement,  $x = +23\text{ mm}$ ,  $y = +2\text{ mm}$ , on the beam pipe and buttons.

The power dissipation  $P_{loss\_metal}$  for each BPM part is then calculated by the energy loss  $\Delta E_{loss\_metal}$  associated to the losses in that specific part

$$P_{loss\_metal} = \frac{\Delta E_{loss\_metal}}{t_{rev}} N_{bunch} \quad (43)$$

assuming a number of  $N_{bunch}$  bunches of equal properties. For simple scaling purposes we always used a bunch charge of  $q_{bunch\_CST} = 1\text{ nC}$  in the *CST Studio* software, which needs

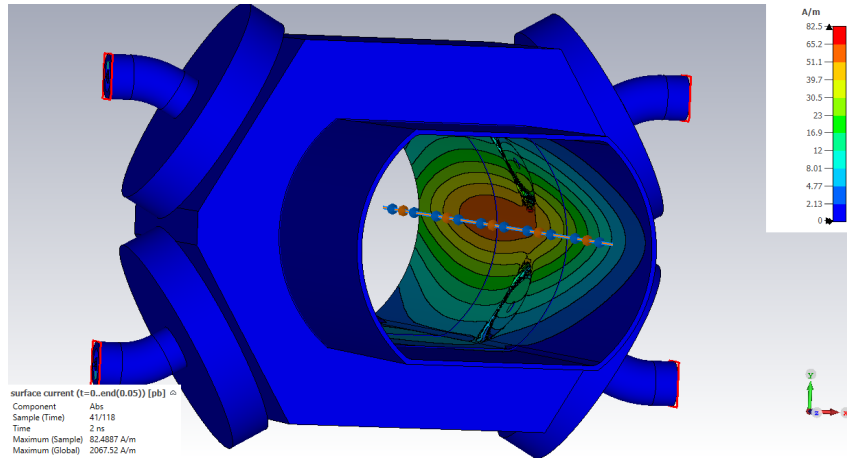


Figure 29. Beam bunch induced surface currents for the HSR corner BPM.

to be scaled as

$$k_{qScale} = \left( \frac{q_{bunch}}{q_{bunch\_CST}} \right)^2 \quad (44)$$

to estimate the actual energy loss in the metallic part, in Eq. (43):

$$\Delta E_{loss\_metal} = k_{qScale} \Delta E_{loss\_metal\_CST} \quad (45)$$

*CST* reports the material or part specific power loss due to the finite conductivity in the metal as power loss vs. time, which needs to be integrated to calculate the associated energy loss:

$$\Delta E_{loss\_metal\_CST} = \int P_{loss\_metal\_CST}(t) dt \quad (46)$$



The power losses due to the H-field induced surface currents are not limited to the beam fields, but for the BPM pickup are also generated by the signal waveforms in the coaxial transmission-lines!

## B. Simulation parameters and other details of the power dissipation analysis

Details and the most important dimensions of the two HSR BPM pickup geometries, along with the materials implemented into the *CST Studio* wakefield analysis are illustrated in Figs. 3a and 3b for the corner BPM button configuration and Figs. 5a and 5b for the orthogonal BPM. Figure 3c shows a more detailed view of the button feedthrough, here for the corner arrangement, indicating the materials used in the *CST* wakefield simulations which are also used for the orthogonal BPM.

Table IV list the parameters used in the numerical simulations and post-processing, assuming the HSR BPM is operated at cryogenic temperatures,  $T \approx 10$  K. While for metals like Inconel 718 or stainless steel 316L the is almost no or only little change in the electrical conductivity compared to operation at room temperature ( $T \approx 300$  K), for copper and the copper-plated surfaces the electrical conductivity changes substantially. Here we use the analytical approximation for the *electrical resistivity* of copper (*Cu*) as function of the ambient temperature ( $T$ ):

$$\rho_{Cu} = \left( \frac{1.545}{RRR} + \frac{1}{\frac{2.32547 \times 10^9}{T^5} + \frac{9.57137 \times 10^5}{T^3} + \frac{1.62735 \times 10^2}{T}} \right) 10^8 + 0.5 \times 10^{10} B \quad (47)$$

assuming no magnetic field at the BPM location ( $B = 0$  T). Figure 30 illustrates Eq. (47),

Table IV. Parameters used of the power dissipation analysis.

beam, machine or material parameter	value
HSR circumference	3833.9 m
revolution time $t_{rev}$	12.7885 $\mu$ s
bunch charge $q_{bunch}$	$19.1 \times 10^{10} \text{ e} = 30.6 \text{ nC}$
number of bunches $N_{bunch}$	290
bunch current $i_{bunch} = q_{bunch} f_{rev}$	2.4 mA
beam current $I_{beam} = i_{bunch} N_{bunch}$	0.694 A
<i>CST</i> specific simulation parameters	
beam velocity $\beta = v/c$	1
simulated bunch charge $q_{bunch\_CST}$	1 nC
bunch length ( <i>Gaussian</i> distribution) $\sigma$	60 mm (200 ps)
max. simulation frequency $f_{max}$	3 GHz
simulated wake length	1000 mm ( $\equiv$ 5.85 ns)
transverse beam locations	$x = 0, +23 \text{ mm}$ ; $y = 0$ and $+2 \text{ mm}$
el. cond. of bulk copper ( $T = 10 \text{ K}$ , $B = 0 \text{ T}$ )	$3.23 \times 10^9 \text{ S/m}$ ( $RRR_{Cu} = 50$ )
SS 316L el. conductivity ( $RRR_{SS} = 1.4$ )	$RRR_{SS} \times 1.25 \times 10^6 \text{ S/m} = 1.89 \times 10^6 \text{ S/m}$
Inconel 718 electrical conductivity	$8.0 \times 10^5 \text{ S/m}$

with  $RRR_{Cu} = \rho_{Cu,300K}/\rho_{Cu,0K}$  being the *residual-resistance ratio* for a given copper quality. Here we assume as default  $RRR_{Cu} = 50$  for the copper bulk material (e.g. the material of the button electrodes) and  $RRR_{Cu} = 10$  for the copper coated (plated) surfaces, like the 316L stainless steel BPM body and beam screen stubs. The electrical resistivity of copper was specified at  $T = 10 \text{ K}$  and given as electrical conductivity  $\sigma_{Cu} = 1/\rho_{Cu}$  in material definition used in the *CST* simulation software.

To include the signal power of the BPM button electrodes dissipated in the read-

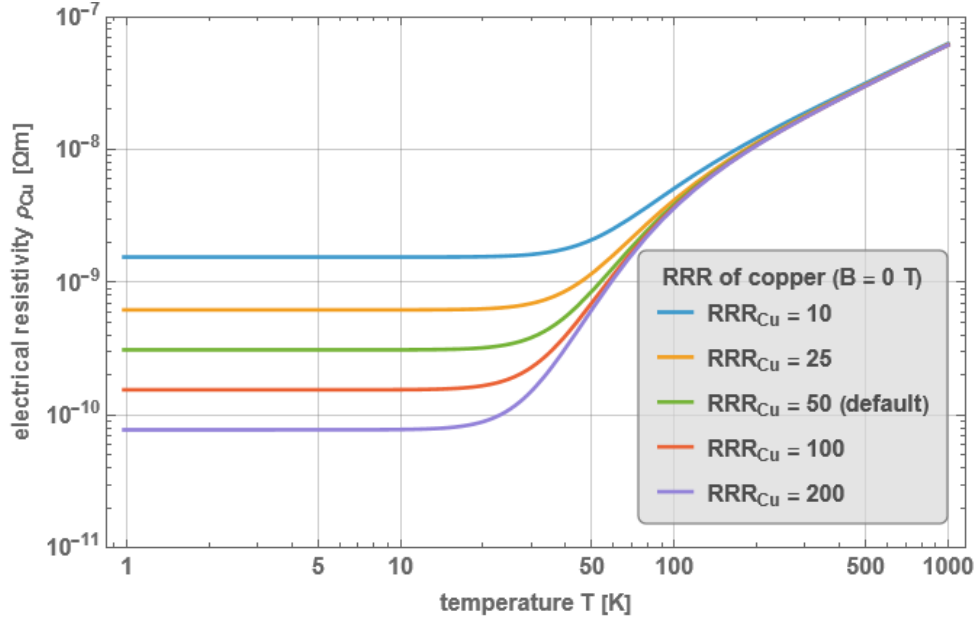
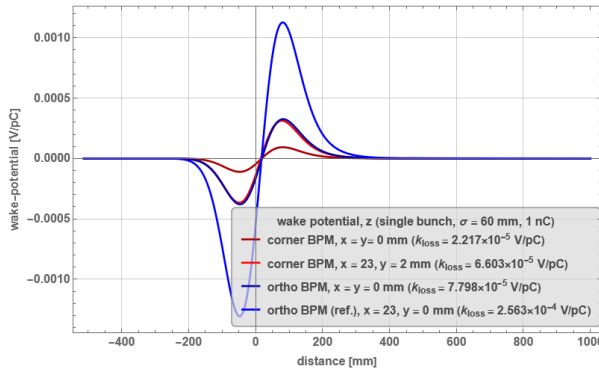


Figure 30. Electrical resistivity of copper vs. temperature (no magnetic field).

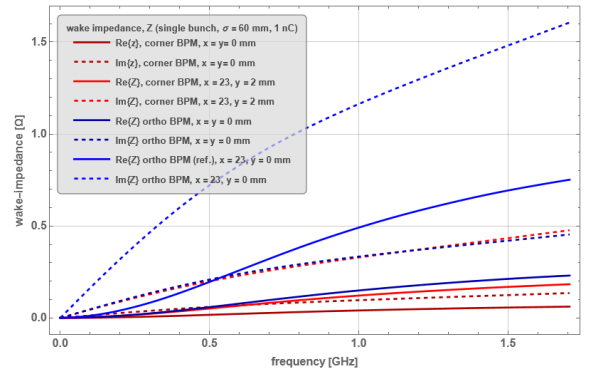
out electronics, *voltage monitors* have been included in the *CST* simulation model. The primary focus of the analysis are the beam and signal induced power losses in the different BPM parts, shown in the cross-sections Figs. 3b, 3c and 5b. For the analysis of those parts we separated the 75 mm long BPM body from the two 87.5 mm long beam screen (beam pipe) stubs, see Fig. 3a.

### C. Results

Figure 31 summarizes the results of the *CST* wakefield solver for the two different HSR BPM geometries, and for each case with the beam centered ( $x = y = 0$  mm) and for a large horizontal displacement, in case of the corner BPM at  $x = +23$  mm,  $y = +2$  mm and in case of the orthogonal BPM at  $x = +23$  mm,  $y = 0$  mm, which we assume as *worst case scenario* wrt. the power losses. Clearly, from a wakefields aspect, the corner BPM performs better than the orthogonal BPM, which is also reflected by the lower loss factor, see the legend in Fig. 31a.



a Wake potential.



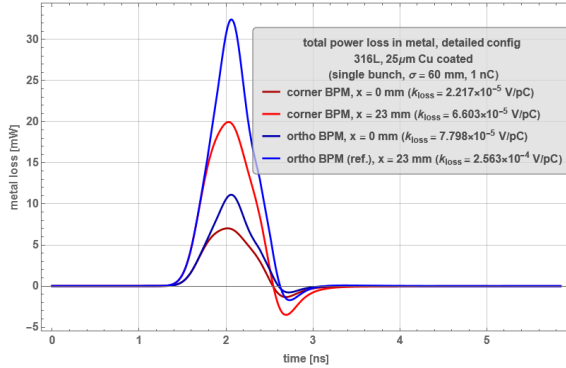
b Wake impedance.

Figure 31. Wake field results from *CST*.

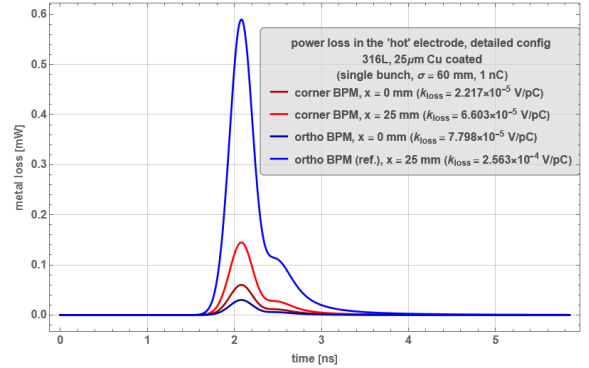


While the maximum simulation frequency was set to  $f_{max} = 3$  GHz, the maximum frequency calculated for the wake impedance (see Fig. 31b) is limited to a frequency equivalent to 10% of the *Gaussian* bunch spectrum spectrum intensity ( $\sim -20$  dB). In our case, for a bunch length of  $\sigma = 60$  mm, this results in a maximum frequency for the wake impedance calculation of approximately 1.7 GHz.

Figure 32 illustrates some examples of the power dissipation  $P_{loss\_CST}(t)$  results from *CST* by monitoring the H-field and surface currents vs. time, as used as input to calculate the dissipated power in a specific part of the BPM pickup Eqs. (43) to (46). Figure 32a shows the total power dissipated in all the metal parts of the BPM (including the two beam pipe stubs), Fig. 32b shows the part dissipated on the “hot” button electrode, i.e.

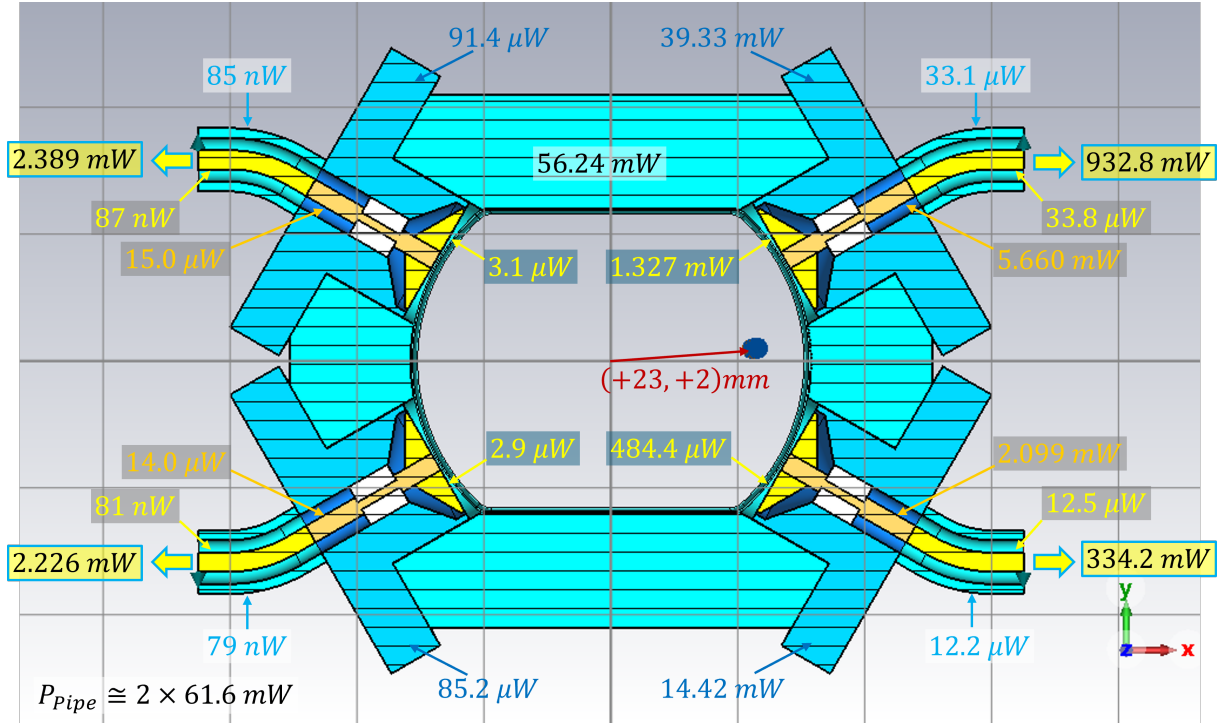


a Losses in all metal.

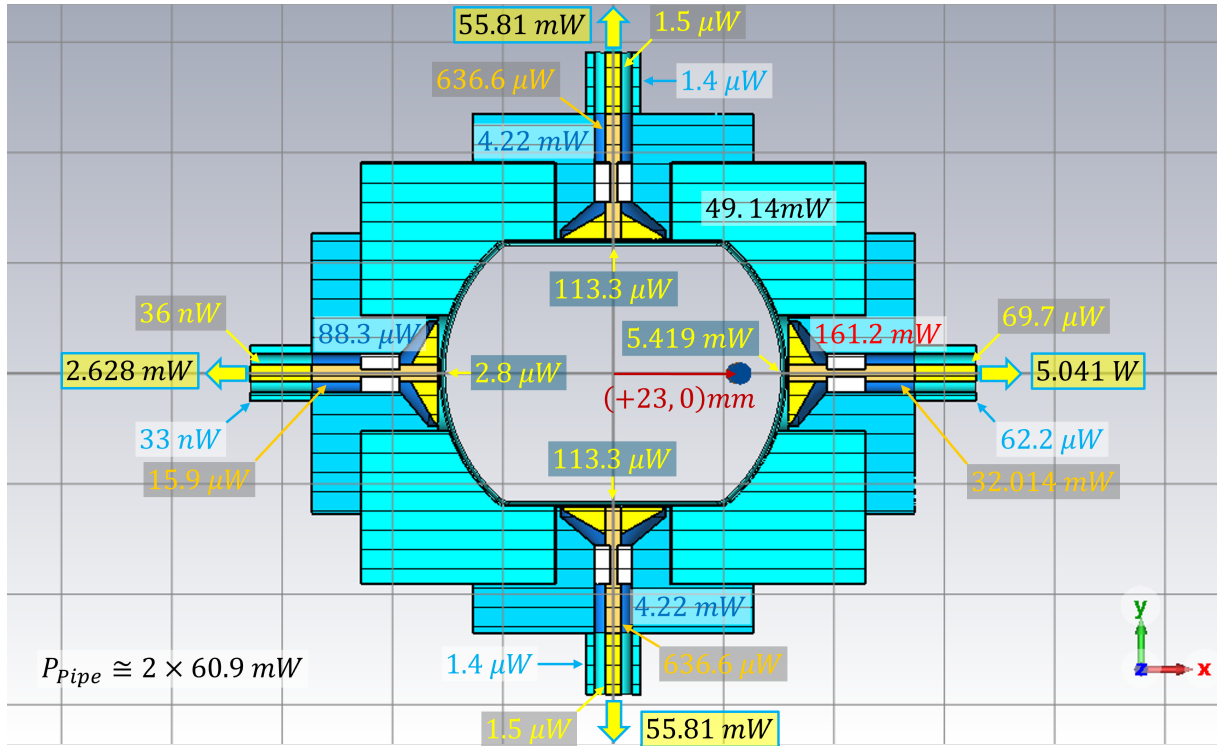


b Losses on the “hot” button electrode.

Figure 32. Power dissipation  $P_{loss\_CST}(t)$  results from *CST*.



a HSR corner BPM.



b HSR orthogonal BPM.

Figure 33. Power loss distribution results for proton beams with large horizontal displacement.

the electrode closest to the beam with large horizontal displacement.



The results of the power loss distribution in the HSR BPM metal parts for beam with large horizontal displacement are summarized in Fig. 33 for both button configurations, and are used as basis for the thermal analysis. The total power losses in the beam field and the power losses distributed in the metals and at the ports should be “almost” identical:

$$P_{loss\_field} \cong P_{loss\_metal} + \sum P_{port} \quad (48)$$

However, some discrepancies are noticeable, Eq. (49):

$$\begin{aligned} P_{loss,corner} &= 1.402 \text{ W} \approx 0.243 \text{ W} + 1.272 \text{ W} = 1.515 \text{ W} \\ P_{loss,ortho} &= \underbrace{5.442 \text{ W}}_{P_{loss\_field}} \approx \underbrace{0.375 \text{ W}}_{P_{loss\_metal}} + \underbrace{5.155 \text{ W}}_{\sum P_{port}} = 5.530 \text{ W} \end{aligned} \quad (49)$$

These differences may have a variety of reasons, e.g. the wakefield simulation could not be performed with the preferred, more accurate *Indirect testbeams* integration method, but has to use the *Indirect interfaces* method. Moreover, the hexahedral meshing of the corner BPM geometry was challenging and unable to accurately approximate the shapes. Also please note that we did not take the losses in the dielectric material of the quartz glass (fused silica) insulator into account.

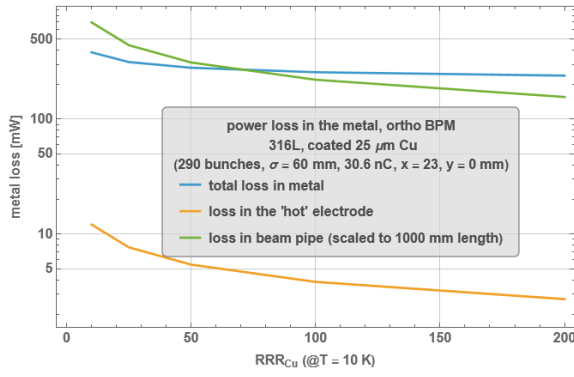
However, Eq. (49) demonstrates, a major fraction of the total field losses are related to the actual needed port signal power (see also Eq. (48)) and may not be viewed as *power losses*. Wrt. to power losses and the associated thermal heating, the power losses in the metal are the relevant part, following Eq. (49) and Fig. 33.



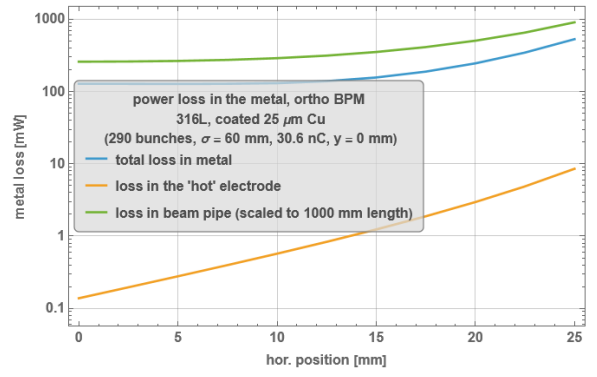
The *CST Studio* wakefield solver requires the ports to be parallel to one of the *Cartesian* coordinates, that is why the coaxial outputs in Fig. 33a are bend towards the yz-plane.



Details of the BPM geometry, materials and coatings are very important for the calculated power loss values! At this point, without the final BPM button feedthrough design at hand, a rather conservative approach was followed, materials with better electrical conductivity or coating could lower some dissipated power substantially, e.g. a copper-beryllium pin instead of Inconel 718, or a copper plating of the 316L stainless steel feedthrough body on the coaxial transmission-line surface.



a As function of  $RRR_{Cu}$ .



b As function of the horizontal beam position.

Figure 34. Power dissipation in the HSR orthogonal BPM and in the beam pipe screen.

The power dissipation results summarized in Fig. 33 uses a “conservative” approach, i.e. using  $RRR_{Cu,bulk} = 50$  for the bulk copper materials (button electrodes) and  $RRR_{Cu,coat} = 10$  for the 25  $\mu\text{m}$  thick coated 316L stainless steel surfaces (BPM body and beam pipe stubs), also using a very large horizontal beam offset ( $x = +23$  mm). Figure 34 illustrates the effect of a change of the  $RRR_{Cu}$  and the horizontal beam displacement on the power losses for the orthogonal BPM, as total power loss in all the metal parts, as power loss on the “hot” (horizontal) button electrode and for comparison the loss in the HSR beam pipe screen, scaled to 1 m length (please note the logarithmic vertical axis!). The  $RRR_{Cu}$  in Fig. 34a was varied to the same values for the bulk and coated copper, here the horizontal beam displacement was kept at  $x = +23$  mm.

## VII. EVALUATION OF THE HSR BPM BUTTON HEATING FOR THE ORTHOGONAL CONFIGURATION

### A. Introduction

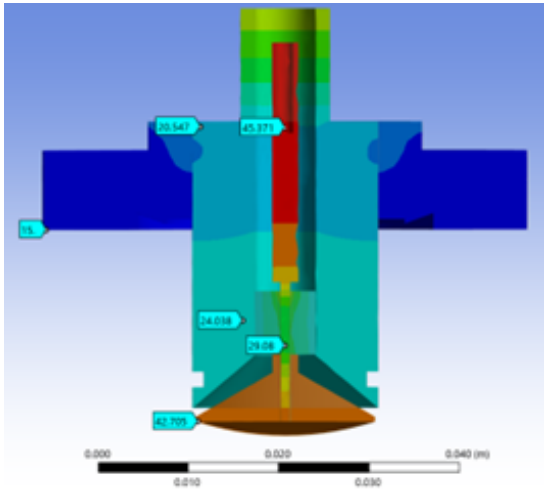
In the original configuration of the HSR BPM the orientation of the button electrodes was  $30^\circ$  up/down from the horizontal plane. This was done to alleviate concerns about heating of the button and ease its mechanical integration in the interconnect. Since the early design, several aspects have reduced the expected button heating, in particular the reduction of the diameter of the button electrodes, from 20 mm to 18 mm, and a change of the material of the buttons itself, from copper-plated stainless steel to pure copper. This, and the significant improvement of the system resolution have motivated a revisit of the heating analysis. FE simulations were conducted to assess the heating of the HSR BPM button in the orthogonal configuration. The general modeling philosophy is described in detail in [1] for the HSR BPM corner button assembly. The following analysis revisits these results for the orthogonal button arrangement.

### B. Heating boundary conditions

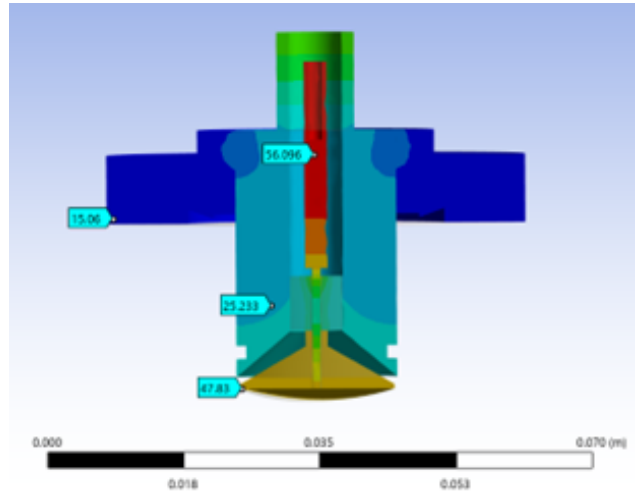
The beam-induced heating as well as the RF power coupled has been obtained through CST simulations, see Fig. 33b and Table VI. The cable attenuation, leading to a heating of the cable, has been obtained through a 1D model developed initially for the button analysis [1, 2]. The BPM housing temperature is estimated to be at 15 K [1].

Table V. Power input values used for the heat analysis (orthogonal BPM).

heat source	estimated power input (mW)
button electrode (bulk copper)	5.4
coaxial outer signal connector (316L button flange)	161
coaxial inner signal connector (Inconel 718)	32
coaxial cable losses ( $\text{SiO}_2$ , 0.141 inch diameter)	376
coaxial cable losses ( $\text{SiO}_2$ , 0.090 inch diameter)	812



a Connected to a 0.141 inch dia. SiO<sub>2</sub> cable.



b Connected to a 0.090 inch dia. SiO<sub>2</sub> cable.

Figure 35. Heating of the HSR orthogonal “hot” button electrode.

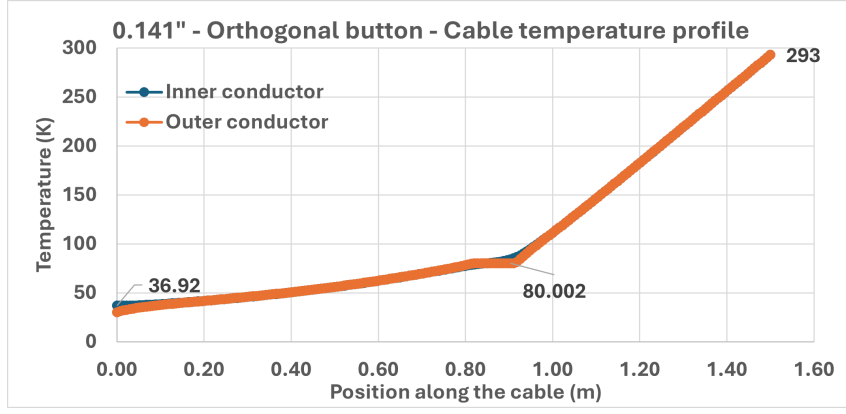
## C. Results

### 1. Button temperature

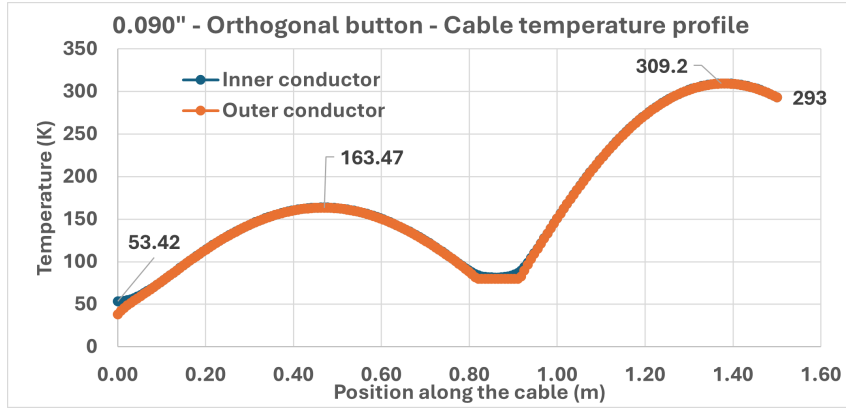
Both cases show a similar response pattern. For the 0.141 inch diameter cable, the button face temperature reaches 43 K. At this temperature, the H<sub>2</sub> desorption from the amorphous carbon (aC) coating face can become a concern. However, upon initial cooling, the BPM module will be kept “hotter” and cooled with a delay compared to the adjacent superconducting magnet, so the H<sub>2</sub> adsorption is expected to be limited on the button face and will be condensed preferentially on the magnet cold bore. The button can also be “baked out” at 80 K along with the beam screen cooling circuit which will help releasing any condensed H<sub>2</sub>.

### 2. Cable temperature

The pattern of the 0.090 inch diameter cable temperature profile is typical of a thermal runaway, see Fig. 36b. While the SiO<sub>2</sub> cable has a high operating temperature, the cable attenuation will vary in time which will affect the BPM output. Therefore, it is not adequate to be used at this high signal power and above.



a 0.141 inch diameter.



b 0.090 inch diameter.

Figure 36. Temperature profile of the  $\text{SiO}_2$  coaxial signal cable.

### 3. Conclusions

In conclusion, provided the potential outgassing of  $\text{H}_2$  at 43 K is acceptable, the use of the HSR BPM button in the orthogonal configuration is granted with the 0.141 inch diameter coaxial cable.

## VIII. SUMMARY

A comparison between two button configurations for the HSR BPMs, under  $\pm 30^\circ$  wrt. the horizontal plane, i.e. the *corner BPM*, and in the horizontal / vertical plane, i.e. the *orthogonal BPM* was presented, mostly based on numerical analysis methods. The focus of the analysis was for bunched beams in HSR collision operation with large horizontal beam displacements, as expected at beam energies of 275 GeV or 100 GeV. While both BPM configurations perform similar at these large  $x \approx \pm 20$  mm beam offset, the orthogonal

Table VI. Power handling summary (orthogonal BPM, 0.141 inch diameter cable).

boundary condition	power input (mW)	power output (mW)
button electrode	5.4	
coaxial outer signal connector	161	
coaxial inner signal connector	32	
coaxial cable losses (0.141 inch dia.)	376	
power from the 293 K feedthrough	133.5	
power to heat shield intercept		-383
power the BPM module (15 K)		-326
<b>total</b>	<b>708</b>	<b>-709</b>

button BPM offers the option to make use of the vertical electrodes as virtual center electrode, which improves the BPM pickup sensitivity and therefore the resolution by  $\sim 4\times$  compared to the corner BPM or the orthogonal BPM not using this “trick”.

Beam and signal induced thermal heating of the “hot” electrode, i.e. the button close to the beam, was a major concern leading to the corner button arrangement. However, those concerns could be mitigated by two measures, reducing the diameter of the button electrodes and using high- $RRR$  bulk copper material for the buttons. Along with the use of 60 inch long, 0.141 inch diameter  $\text{SiO}_2$  semi-rigid coaxial signal cables between button output and insulation vacuum feedthrough, the thermal heating is manageable also under the most extreme HSR operating condition (hor. beam offset: 23 mm,  $q_{\text{bunch}} = 30.6 \text{ nC}$ ,  $N_{\text{bunch}} = 290$ ).

---

## SUPPLEMENTARY REFERENCES

- [1] *F. Micolon, et.al.*, “Thermal simulation of the HSR arc BPM for EIC”, BNL technical report BNL-224218, 2023-TECH, DOI: 10.2172/1969913
- [2] *F. Micolon, et.al.*, “Thermal engineering of the cryogenic beam position monitors for the EIC hadron storage ring”, Proceedings of the Cryogenic Engineering Conference (CEC23) proceedings, DOI: 10.1088/1757-899X/1301/1/012152\_